MEASUREMENT OF CHARGED-CURRENT ν_μ AND ν_e INTERACTIONS WITH WIRE-CELL IN MICROBOONE TOWARDS A SEARCH FOR LOW-ENERGY ν_e EXCESS

February 18, 2021

The MicroBooNE collaboration
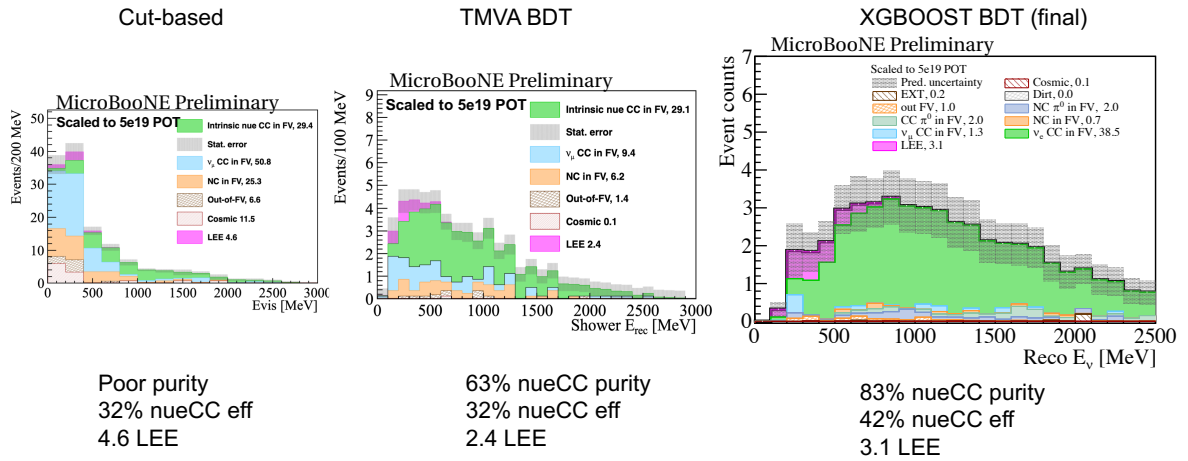microboone_info@fnal.gov

Abstract

This technote summarizes the existing work in searching for ν_e low-energy excess (eLEE) in MicroBooNE Booster Neutrino Beam (BNB) data stream based on the Wire-Cell event reconstruction paradigm. The charged-current ν_μ and ν_e events are selected from the 5.3e19 POT data from the BNB beam and 2.06e20 POT data from Neutrinos at the Main Injector (NuMI) beam. The charged-current ν_e selection results from the BNB data that are sensitive to the eLEE search are not included. Various comparisons between data and Monte Carlo predictions are performed to validate the overall model and demonstrate the power of the analysis techniques.

Contents

1 INTRODUCTION

This technote summarizes some foundational work for a low-energy ν_e excess (eLEE) in MicroBooNE [1] using the Wire-Cell event reconstruction paradigm. The starting point of this analysis is the generic neutrino detection [2, 3, 4], in which the cosmic-ray backgrounds are largely rejected resulting an overall contamination level below 15%. After the generic neutrino selection, the efficiencies for selecting charged-current ν_μ (ν_μCC) and ν_e (ν_eCC) events are about 80% and 90%, respectively. The signal-to-background ratios for ν_μCC and ν_eCC are about 2:1 and 1:190, respectively, and are further improved with the techniques described in this technote. The event selections in this analysis are designed to be as general as possible (i.e. inclusive ν_eCC and ν_μCC event selections), so that more freedom is available at later stages of the analysis if an excess is observed.

Figure 1: Evolution of the ν_eCC event selection from human learning/engineering to machine learning. The combination of generic features selected by human engineering and high statistics simulation events evaluated by the machine learning yields a robust and high-performance ν_eCC event selection.

As shown in Fig. 1, the development of the ν_eCC event selection (or tagger) naturally follows a transition from human learning/engineering to machine learning. During the human learning stage, hand scan techniques are used to identify generic features that can be used to perform event selection. The features are intended to be robust against the detailed simulation/data differences. Although the hand scan is efficient in selecting generic features, it is clearly limited by the capacity of a human being. For example, a person can generally study only about 20 events in details per day. While this capability is enough for a task with a reasonable initial signal-to-background ratio (i.e. ν_μCC at 2:1), it is not sufficient for a task with a poor initial signal-to-background ratio (i.e. ν_eCC at 1:190). For the latter, machine

learning techniques are necessary, since hundreds of thousands of simulated events can be studied by a computer at once. In particular, we use a boosted decision tree (BDT) trained on the generic features that were engineered by the hand scan to maximize the efficiency and purity of final ν_eCC and ν_μCC event selections. A purity of 83% (93%) and an efficiency of 42% (64%) are achieved for ν_eCC (ν_μCC) event selection. Together with the evolution of ν_eCC event selection, the energy reconstruction has also evolved from the visible energy to the EM shower energy, and then to the reconstructed neutrino energy, which has the best resolution and capability to distinguish signal and background events.

Test Statistics based on Covariance Matrix

$$\chi^2 = \left(M - P\right)^T Cov\left(M, P\right)^{-1} \left(M - P\right)$$

M: measurement vector
P: prediction vector

	Nested Likelihood Ratio	Simple-vs-simple Likelihood ratio	Goodness-of-fit
Test statistics	$\Delta\chi^2_{nested} = \chi^2\left(x = x_0\right) - \chi^2_{\min}\left(x_{\min}\right)$	$\Delta\chi^2_{nested} = \chi^2_{SM} - \chi^2_{LEEx=1}$	χ^2_{SM}
Chi-square	CNP	CNP	Pearson
Motivation	Rejection/compatibility of the null hypothesis, construction of confidence interval	Compatibility of the null hypothesis, rejection of new-physics hypothesis	Compatibility of the null hypothesis
Special features	Non-negative x, Feldman-Cousins approach	Frequentist approach for p-value calculation	Conditional covariance matrix for selected channels

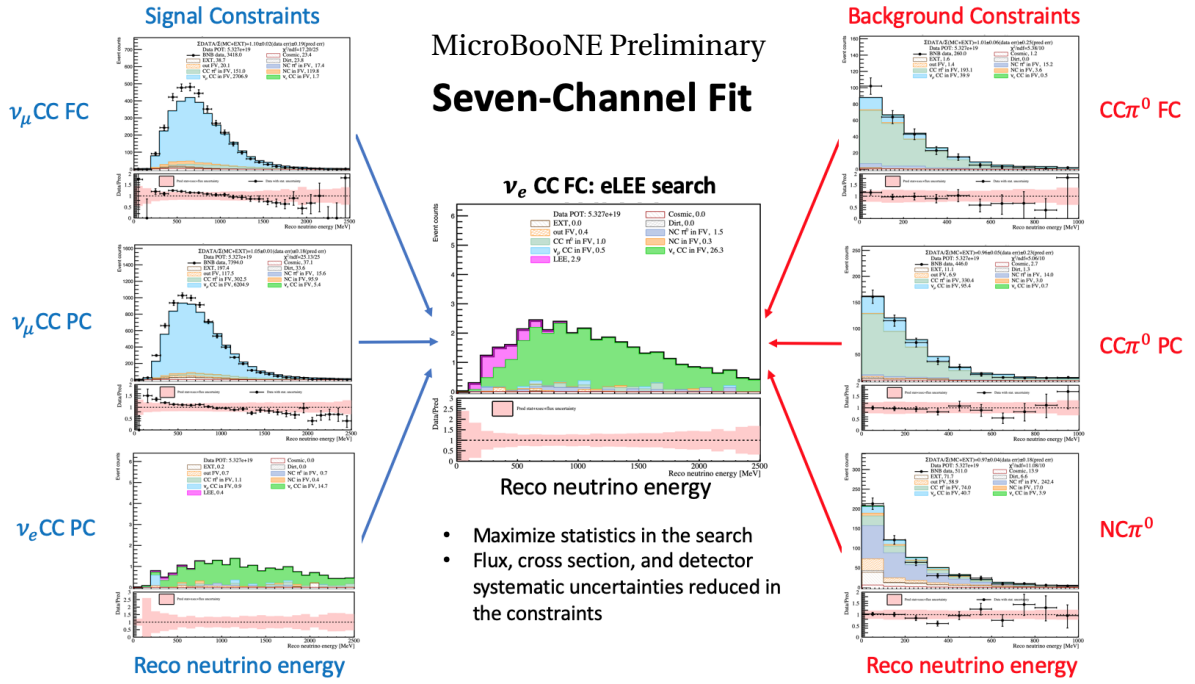CNP: Combine-Neyman-Pearson Chisquare,   NIMA 961, P163677
Feldman-Cousins: Phys.Rev.D57:3873-3889
Conditional Covariance Matrix: Eaton, Morris L. (1983)

Figure 2: Summary of test statistics used in this analysis.

The search for an LEE signal is equivalent to testing the null hypothesis defined as the Standard Model (SM) prediction without an LEE signal. The SM prediction is formed based on state-of-art understanding of the Booster Neutrino Beam flux [5], the neutrino-argon interaction cross section [6], detector simulation [7, 8, 9], and signal processing [7, 10, 11, 12]. The alternative hypothesis is formed based on a model of a potential anomalous enhancement in the rate of intrinsic ν_eCC events at true neutrino energies less than 600 MeV with a fixed spectral shape. The model is obtained by unfolding the observed excess of electron-like events in MiniBooNE [13] to true neutrino energy under a charged-current quasi-elastic (CCQE) hypothesis and applying that directly to the rate of intrinsic ν_eCC events expected in MicroBooNE [14]. In the alternative hypothesis, we allow the normalization of this low energy excess model to float and define a signal strength parameter x, such that $x = 0$ corresponds to no anomalous enhancement in the expected rate of intrinsic ν_eCC events (the SM case)

and $x = 1$ corresponds to an anomalous enhancement in the expected rate of intrinsic ν_eCC events of equal magnitude to that obtained from the unfolded MiniBooNE measurement (or $LEE\,x = 1$).

We fit this model to our data by minimizing a χ^2 test statistic that incorporates our knowledge of experimental uncertainties and their correlations into a covariance matrix and obtain a best fit value of $x = x_{min}$. We compute the $\Delta\chi^2_{nested}$ for our data for each value of the signal strength x, relative to this best fit point, and obtain frequentist confidence intervals for the signal strength x following the Feldman-Cousins unified approach [15]. This test is essentially a nested likelihood ratio (LR) hypothesis test. In addition to the primary nested LR test statistics ($\Delta\chi^2_{nested}$), several other test statistics are used to provide supplemental information. They are i) goodness-of-fit (GoF) based on a Pearson χ^2; and ii) a simple-vs-simple likelihood ratio test ($\Delta\chi^2_{simple} = \chi^2_{SM} - \chi^2_{LEE\,x=1}$), which provides additional information regarding the tests against the null hypothesis. Figure 2 summarizes the various test statistics used in this analysis.

Figure 3: Illustration of the 7-channel fit in searching for eLEE. All plots can be found in Sec. 6. Data points for ν_e CC selection are not available.

To maximize the physics sensitivity of this search, a 7-channel fit strategy is adopted as shown in Fig. 3. The seven channels are i) fully contained (FC) ν_eCC, ii) partially contained (PC) ν_eCC, iii) fully contained ν_μCC, iv) partially contained ν_μCC, v) fully contained CCπ^0,

vi) partially contained $CC\pi^0$, and vii) $NC\pi^0$. The primary channel that is sensitive to the LEE search is the FC ν_eCC. Three channels — PC ν_eCC, FC ν_μCC, and PC ν_μCC — are used to provide constraints to the signal prediction (e.g. neutrino flux, cross section, and detector systematics). The other three channels — FC $CC\pi^0$, PC $CC\pi^0$, and $NC\pi^0$ — are used to improve the background prediction, since π^0's are one of the major backgrounds of ν_eCC events. To ensure these seven channels are statistically independent, the event selections are designed to be exclusive from each other. For example, the $CC\pi^0$ event selection excludes the ν_eCC candidates. Similarly, the ν_μCC event selection excludes ν_eCC and $CC\pi^0$ candidates. In the 7-channel selection plots shown in this note, the categories "ν_μCC" and "NC" exclude ν_eCC and π^0 events.
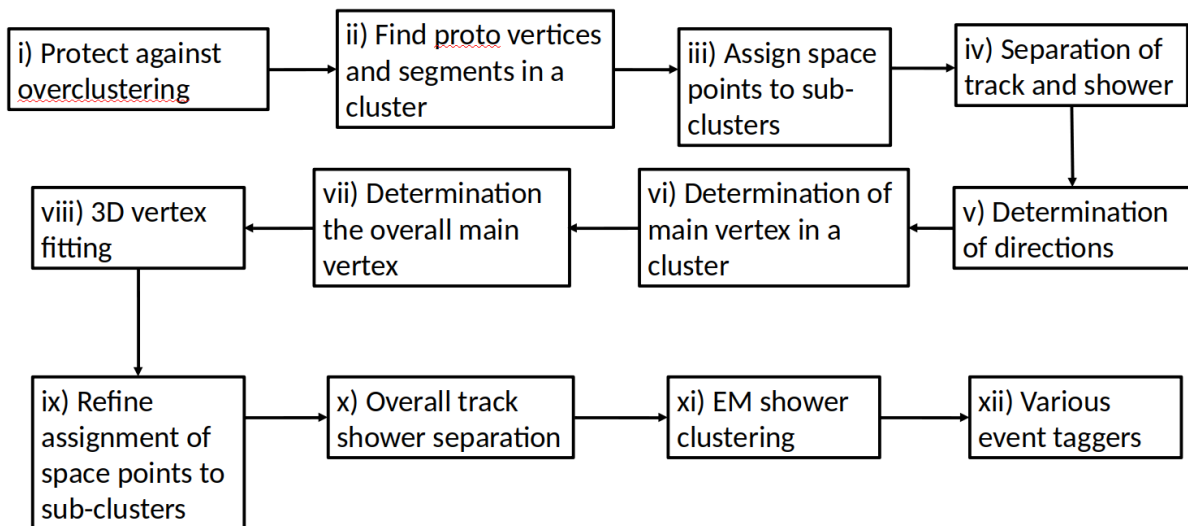
In this analysis, we consider the various sources of systematic uncertainties from i) neutrino flux of the Booster Neutrino Beam, ii) the neutrino-argon cross section based on the GENIE event generator, iii) detector performance, iv) finite statistics from Monte Carlo simulation, and v) additional uncertainties. Different sources of systematic uncertainties have different impacts on the predicted event distributions. The systematic uncertainties associated with the neutrino flux would change the distribution of events by providing different weights for events with different true neutrino energy and flavor. The systematic uncertainties of cross section and detector performance can impact the efficiency (for both signal and background) as well as the reconstruction of kinematic variables. The uncertainty because of the limited statistics of Monte Carlo simulation is particularly important for rare event searches (e.g. ν_eCC). Additional uncertainties are necessary for estimating systematics for the background contributions from neutrino interactions originating outside the cryostat (subsequently referred to as DIRT events).

2   WIRE-CELL PATTERN RECOGNITION

This section summarizes the development of the pattern recognition techniques in Wire-Cell, which are the foundation of the high-performance ν_eCC and ν_μCC event selections. Some of the basic tools—the track trajectory and dQ/dx fitting used to reject stopped muons, for example—are improved versions of techniques developed for the generic neutrino detection [16]. This fitting algorithm was expanded to fit multiple tracks with vertices connecting them rather than fitting a single track. Figure 4 shows the overall flow of Wire-Cell pattern recognition. We summarize the pattern recognition strategy briefly here. First, vertices are defined by searching for kinks and splits in the reconstructed 3D images. With vertices determined, segments between vertices are defined. A 3D vertex fitting technique is then used
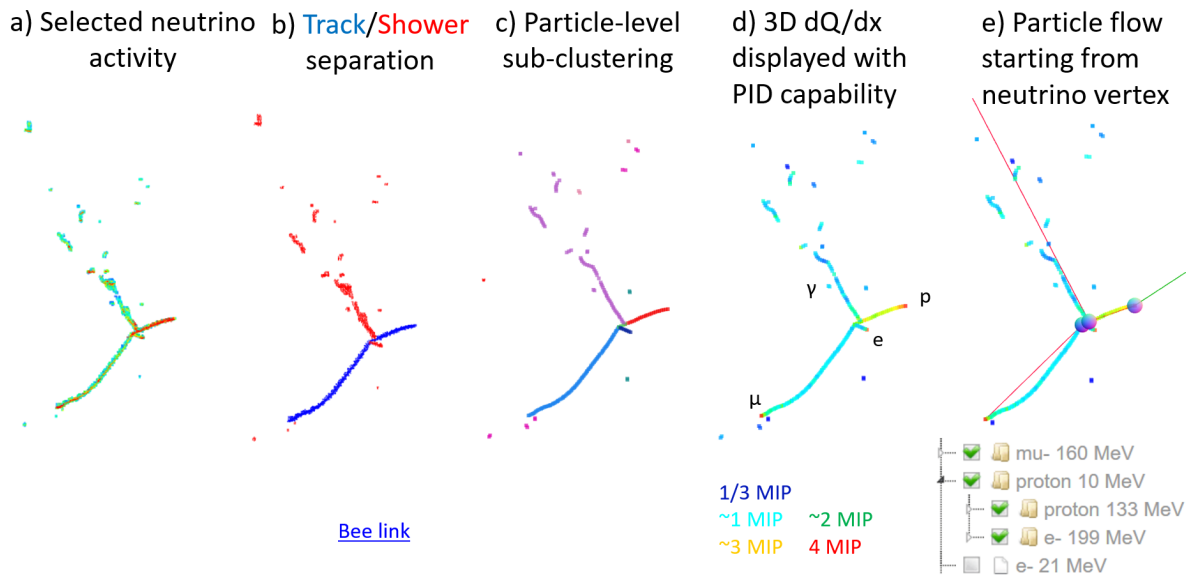
to refine the position of 3D vertex. Particle identifications (PID) is subsequently performed on segments using dQ/dx and event topology information. Event topology information is primarily targeted toward electromagnetic (EM) shower identification (i.e. track/shower separation). Using particle identification information, the direction of the particles can be determined in many cases, which is very useful in determining the primary neutrino interaction vertex. In parallel, we also use deep learning techniques to determine the primary neutrino vertex. With the neutrino interaction vertex reconstructed, one can then fully cluster EM showers, which often encompass several separated sub-clusters. Finally, one can reconstruct π^0s from EM showers.

Overview of Wire-Cell Pattern Recognition

Figure 4: Overview of the Wire-Cell pattern recognition procedure. More details can be found in the text.

Figure 5 illustrates the results of the pattern recognition at different stages. dQ/dx information is especially important for particle identification and determining the direction of particle trajectory. The current labels (e^-, μ^-, π^+) are only temporary and include their respective counterparts (e^+, μ^+, π^-) as well. In the event shown in Fig. 5, the EM shower connecting to the primary proton is produced by a gamma instead of by an electron with high dQ/dx at the beginning of the EM shower. However, it is still displayed as an electron as a proxy for EM showers before a detailed e/gamma separation.

Figure 5: Results of the Wire-Cell pattern recognition are displayed at different stages. The candidate neutrino activity selected by the generic neutrino detection step is shown in Fig. 5a, in which the color represents the reconstructed charge in 3D. The identified tracks and EM shower are displayed in blue and red, respectively, in Fig. 5b. The different identified particles (or segments) are displayed in different colors in Fig. 5c. The determined 3D dQ/dx information with the multi-track trajectory and dQ/dx fitting algorithm is shown in Fig. 5d. The blue, cyan, green, yellow, and red colors roughly represent 1/3, 1, 2, 3, and 4 times of dQ/dx of a minimal ionizing particle (MIP), respectively. Finally, the particle flow information starting from the determined primary neutrino interaction vertex is shown in Fig. 5e. The original BEE weblink is `https://www.phy.bnl.gov/twister/bee/set/uboone/reco/2021-01/pr-1/event/3/`.

2.1   Neutrino Energy Reconstruction

For eLEE search, the reconstruction of neutrino energy is particularly important. Three methods are used to calculate the energy of the reconstructed particles:
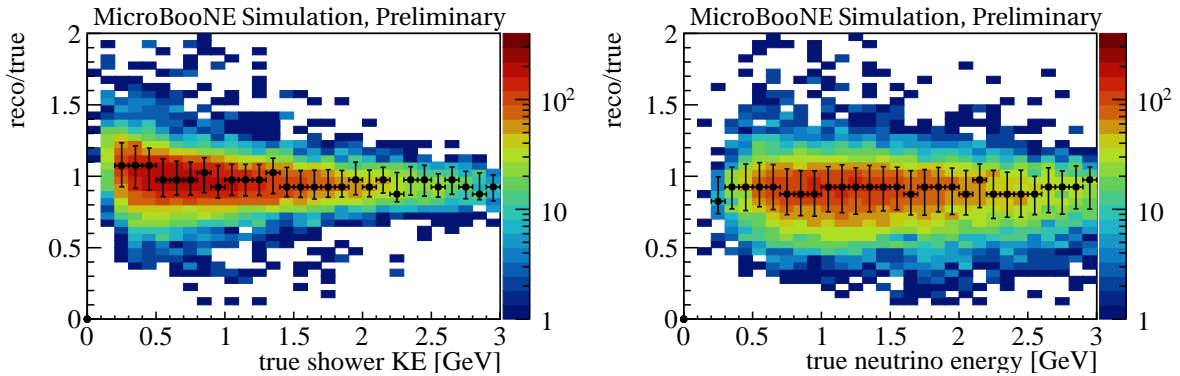
- Range: the travel range of a track-like object can be used to calculate the energy of the particle if it stops inside detector. The NIST PSTAR database [17] is used to derive the relation between the range and the kinetic energy of each particle type (different particle mass).

- dQ/dx corrected by the recombination effect: the ionization charge per unit length dQ/dx is connected to the energy loss per unit length dE/dx through the recombination model. Therefore, by performing a charge recombination correction, we can convert the measured dQ/dx to dE/dx, which can be used to derive the energy of the particle. We use the recombination model published in Ref. [9] to perform such

a correction. This method can be used for both stopped particles as well as particles exiting the detector.

- Charge scaling: while the above two methods are good for track-like object, they are not suitable for EM showers because of the difficulties in deriving dQ/dx or range. For EM showers, the energy is estimated calorimetrically by scaling the total charge information: $Q/0.4$. This factor is derived from MC study including the bias in the reconstructed charge [18] and the average recombination factor ($\approx$0.5) of an EM shower.

For a stopped track longer than 4 cm, range is used to estimate energy. For short stopped tracks (< 4 cm), the dQ/dx with recombination correction is used to estimate energy. For EM showers, charge scaling is used to estimate energy. In addition, an average 8.6 MeV binding energy is added for each identified proton in the reconstructed particle flow. These protons may be produced at the primary neutrino interaction or secondary interactions (e.g. produced by a neutron). For each muon, charged pion, or electron, its mass is added to the energy reconstruction. Fig. 6 illustrates the performance of the neutrino energy reconstruction. The reconstructed neutrino energy resolution is 10%-15% for ν_eCC across the entire energy region. Typically, the reconstructed neutrino energy resolution is 15% at the truth neutrino energy of 800 MeV. In comparison, the reconstructed EM shower energy resolutions are 14%, 13%, 12% for truth EM shower energy 200 MeV, 400 MeV, and 800 MeV, respectively.
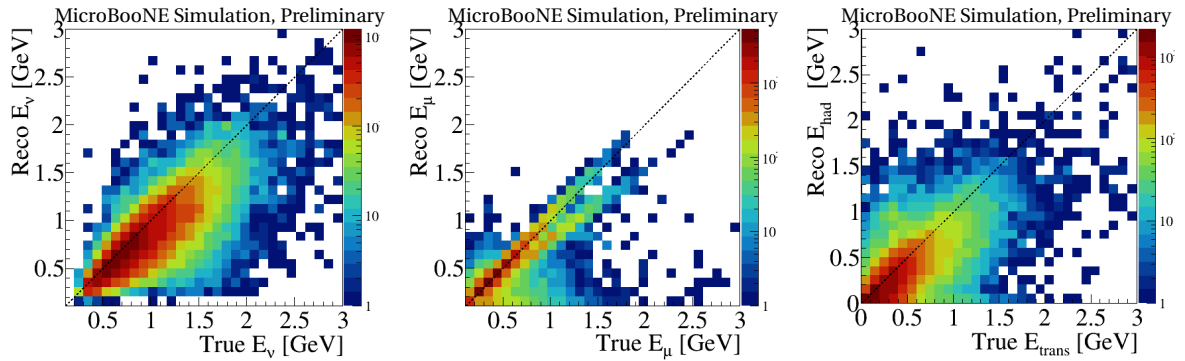

Figure 6: Ratio of reconstructed shower or neutrino energy to truth for fully contained ν_e CC candidates with actual BDT selection (Sec. 4). The peak values and the corresponding resolutions (asymmetric, 68.27% quantile from the peak value on either side) for each true energy bin are plotted as well. Overall, the energy resolutions of shower and neutrino reco energies are about 12% and 15%, respectively.

Dedicated studied are carried out to validate the reconstruction of neutrino energy. The dQ/dx with recombination correction method is validated by comparing the dQ/dx vs.
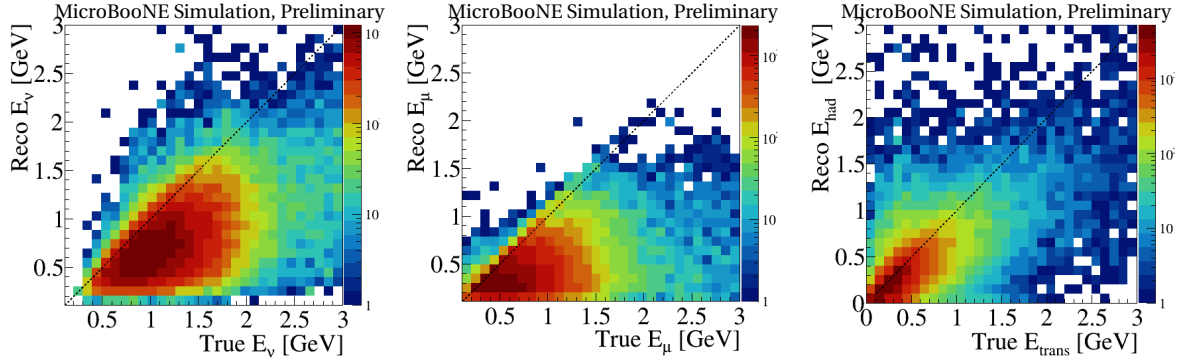
residual range for the stopped muons and protons between data and Monte Carlo (see Fig. 31). The energy reconstruction of EM showers is validated by comparing the reconstructed π^0 mass between data and Monte Carlo (see Fig. 32). The accuracy of the reconstructed neutrino energy also depends on the the modeling of the neutrino-argon interaction, which is validated in Sec. 6.1. In addition to the reconstructed neutrino energy (E_ν^{rec}), we also introduce a few useful intermediate kinematics variables:

- E_μ^{rec}: total reconstructed energy of the primary muon including the muon mass. The reconstruction of this energy is based on the reconstructed kinetic energy of the muon K_μ^{rec}. E_μ^{rec} is directly linked to the true muon energy E_μ.

- θ_μ^{rec}: reconstructed polar angle of the primary muon with respect to the incident neutrino beam direction. θ_μ^{rec} is derived from the reconstructed direction of the primary muon. This variable is directly linked to the true muon polar angle θ_μ.

- E_{had}^{rec}: total reconstructed energy of the hadronic energy system, which is essentially the difference between E_ν^{rec} and E_μ^{rec}. This variable is linked to the energy transfer to the Argon system $\nu = E_\nu - E_\mu$.

These definitions are crucial to validate the reconstruction of neutrino energy in Sec. 6.1.

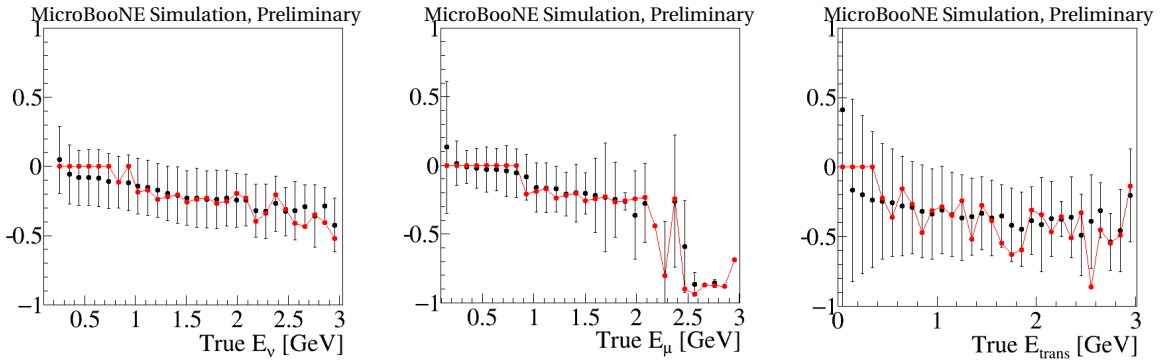

Figure 7: Fully contained ν_μCC candidates: (left) true neutrino energy vs. reconstructed neutrino energy, (middle) true muon energy vs. reconstructed muon energy, (right) true transferred energy to the Ar system vs. reconstructed hadronic energy.
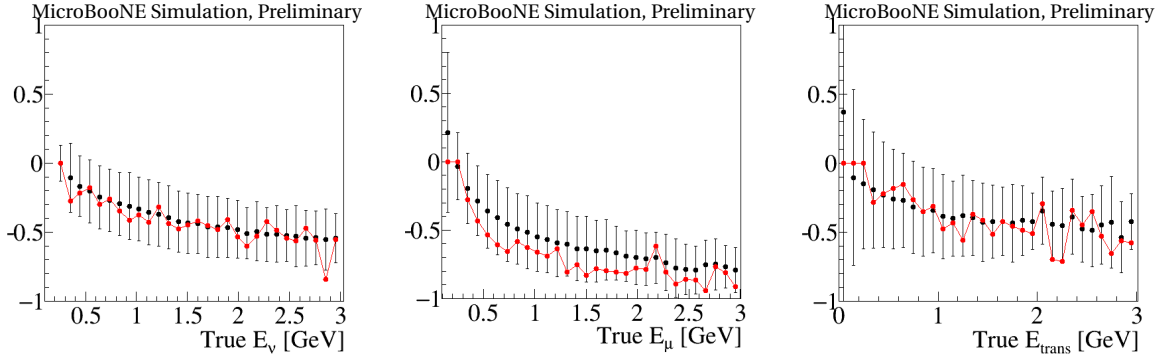
Figure 8: Similar as in Fig. 7 but is for partially contained candidates.

Figure 7 shows the reconstruction performance for various energies for the FC ν_μCC candidates. Long muons are vulnerable to delta-ray radiation and multiple scattering, and therefore, are more easily to be broken and segmented into several clusters in the pattern recognition, in which we estimate muon energy with a dedicated recombination model. However, this model predicts 20% less energy than the ones in both data and MC. As a reuslt, a bias in the reconstructed muon energy can be observed, as shown in Figure 7 (middle). This can be improved in the next round of data production. Figure 9 shows the corresponding bias and resolution below 3 GeV. Figure 8 and Fig. 10 show the similar results for PC ν_μCC candidates. The overall resolution for the reconstructed neutrino energy for the ν_μCC selection is about 20%.

Figure 9: Fully contained ν_μCC candidates: relative bias of the reconstructed energy below 3 GeV for (left) neutrino energy, (middle) muon energy and (right) hadronic energy. The black points indicate the relative bias derived from the 50% quantile, and the associated error bars is combined from the 16% and 84% quantiles. The red points are the relative biases independently calculated from the maximum bin of the reconstructed energy distribution, and is used as a cross check. The two metrics for bias are mostly consistent.
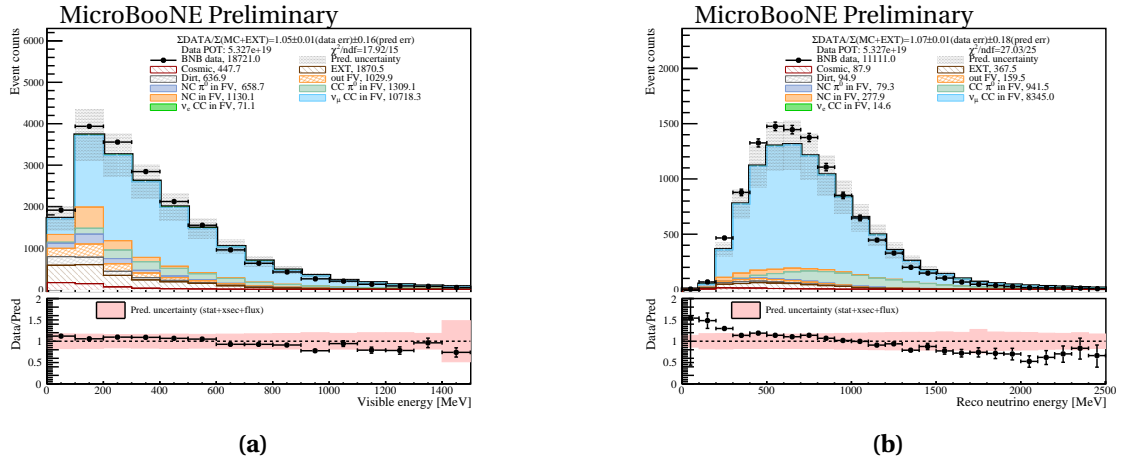
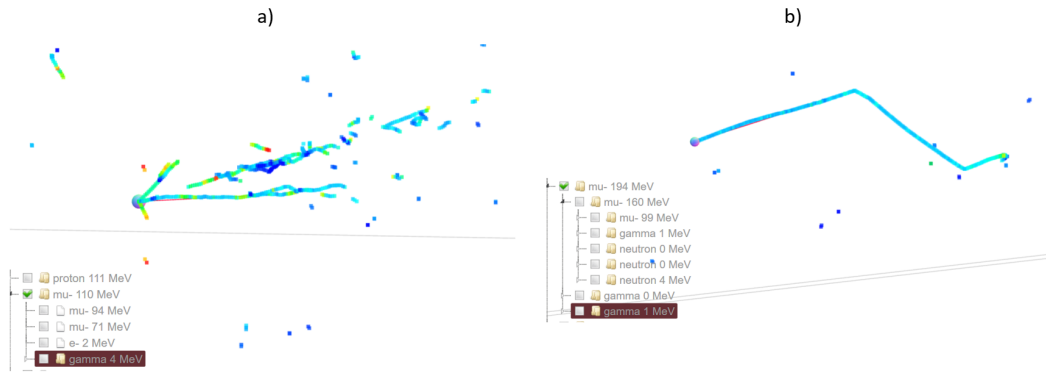**Figure 10:** Similar as in Fig. 9 but is for partially contained candidates.

3 CHARGED-CURRENT ν_μ SELECTION

When doing a ν_μCC event selection in MicroBooNE, a surface-operating LArTPC, the primary challenge is the removal of cosmic-ray muons. Wire-Cell generic neutrino detection [16, 2, 3, 4] does a significant portion of the work to remove cosmic background events. Figure 11a shows the result after generic neutrino detection, of which ~65% are ν_μCC events with an efficiency about 80%. Cosmic-ray muons are reduced to below 15% of the remaining events. With additional pattern recognition techniques developed in Wire-Cell, an improved ν_μCC selection with a purity of ~90% and efficiency of ~65% is achieved (see Fig. 11b) by further rejecting neutral-current events through requiring a reconstructed muon to be longer than 5 cm and removing the residual cosmic-muon backgrounds. Figure 12 shows various residual backgrounds entering the detector from outside. Figure 13 shows example mistakes where a muon is misidentified as a charged pion. In Fig. 13a, the muon was misidentified because of the overlap with an EM shower. In Fig. 13b, the muon has several large-angle scatterings. Figure 14 shows examples where NC events are misidentified as ν_μCC interactions. In both cases, a charged pion behaves like a muon (e.g. no rescattering).
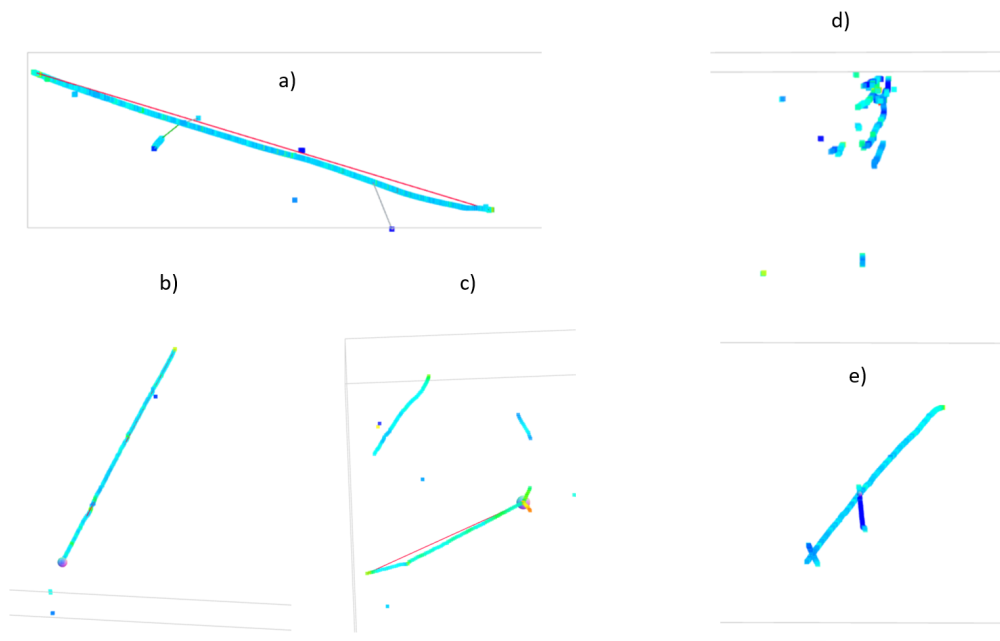
We further developed a ν_μCC event selection based on the modern Boosted Decision Tree (BDT) library: XGBoost [19]. Along with other improvements in vertex finding and energy reconstruction, ~93% purity and ~64% efficiency were achieved. Figure 15 shows the final BDT ν_μCC selections, scaled to 5E19 POT, for fully contained and partially contained samples. Figure 16 shows the selection efficiency for the ν_μCC interactions in the active TPC volume as functions of true neutrino energy (E_ν), true muon energy (E_μ), and true transferred energy to argon nucleus ($E_\nu - E_\mu$), respectively.

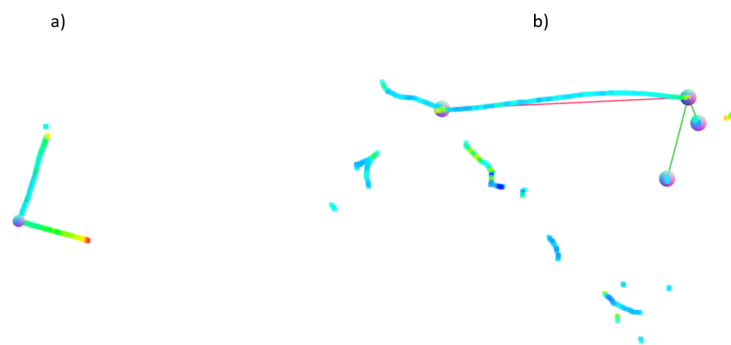**(a)**   **(b)**

Figure 11: Cut-based ν_μCC selection. The left panel shows the result after generic neutrino detection where $\sim 2/3$ of the events are already ν_μCC with an efficiency of about 80%. The right panel shows the cut-based ν_μCC selection where 90% of the events are ν_μCC with an efficiency of about 65%.
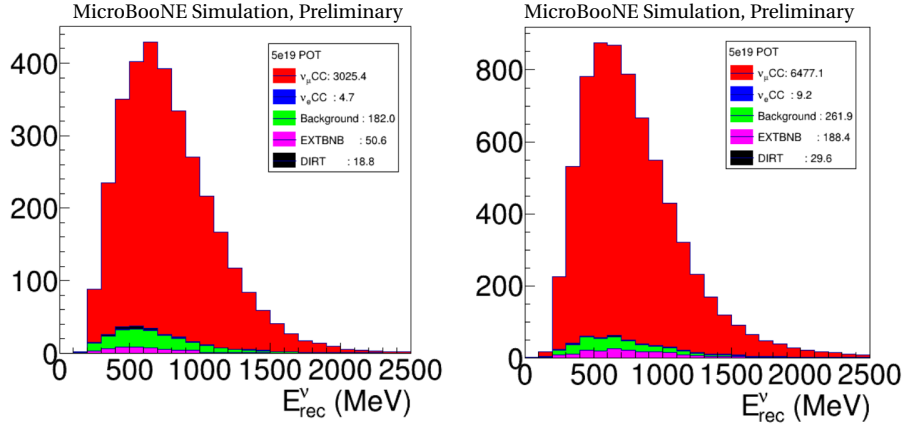

Figure 13: ν_μCC events misidentified as NC backgrounds. (Left) the charged muon is misidentified as a charged pion because of its overlap with an EM shower. (Right) the charged muon is misidentified as a charged pion because of several large-angle deflections. The grey box represents the MicroBooNE active TPC volume, which is 2.56 m in the drift direction (X), 2.3 m high (Y), and 10.56 m along the beam axis (Z).

Figure 12: Various backgrounds for the ν_μCC selection (both comsic and neutrino-induced) originating from outside the detector fiducial volume: a) reconstructed neutrino vertex is outside the fiducial volume; b) a single muon with an incorrect matched light signal, which can be confused as a single muon going out of the detector; c) part of a neutrino interaction going into the detector from the upstream; d) only part of a EM shower can be seen at the top of the detector; e) a single muon with some ghosts tracks (part of Michel electron identification). The grey box represents the MicroBooNE active TPC volume, which is 2.56 m in the drift direction (X), 2.3 m high (Y), and 10.56 m along the beam axis (Z).
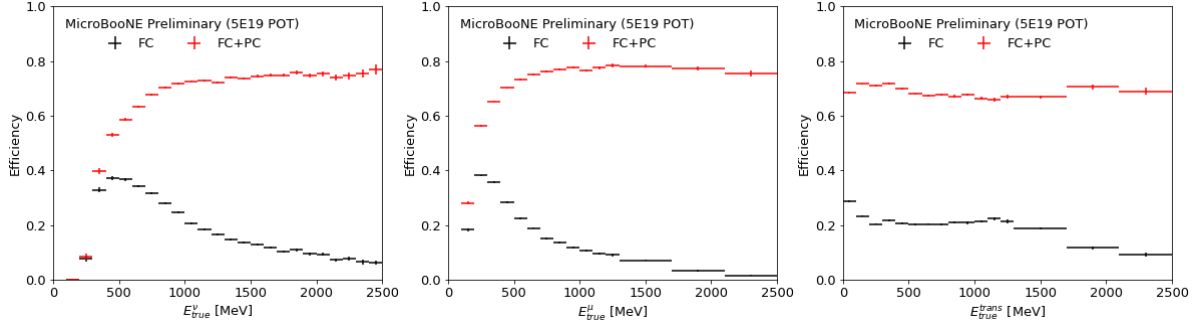

Figure 14: NC events misidentified as ν_μCC. In both cases, the charged pion behaves like a muon.

Figure 15: The final BDT ν_μCC selections, scaled to 5E19 POT, for fully contained and partially contained samples.

Figure 16: Efficiency of the ν_μCC selection in the active TPC volume as functions of true neutrino energy, true muon energy and true transferred energy to Ar, respectively. Both FC and FC+PC event selections are shown in the figures.
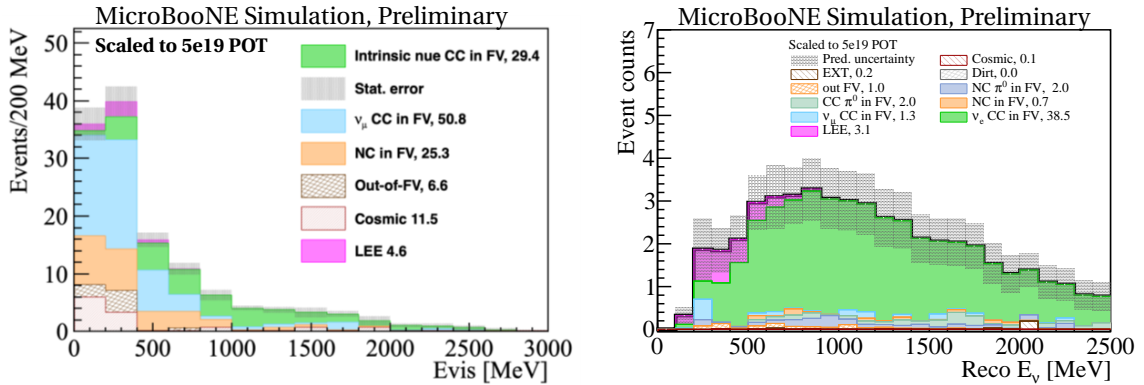
3.1 Charged-Current/Neutral-Current π^0 Selection

The charged-current ν_μ selection described above can be used to create a charged-current π^0 selection to be used as a data-driven constraint of the charged-current π^0 backgrounds for ν_eCC event selection. Additionally, a neutral-current π^0 selection can be achieved by considering only events not selected by the charged-current ν_μ selection described above. In reconstruction π^0, the γ pair pointing to the same vertex with highest energies are chosen. The primary π^0 is ensured by placing a distance cut between the neutrino vertex and π^0 vertex. Further selection cuts use the γ energies and distances from the neutrino vertex, as well as the angle between the two γ's, and the reconstructed π^0 invariant mass. The comparison between data and MC on the reconstructed π^0 mass can be found in Fig. 32.

4   CHARGED-CURRENT ν_e EVENT SELECTION

Compared to ν_μCC interactions, the selection of ν_eCC interactions is much more challenging. While the signal-to-background ratio of ν_μCC interaction is about 2:1 after the generic neutrino detection [16], the signal-to-background ratio of ν_eCC interaction is about 1:190. In the ν_μCC selection, the application of pattern recognition techniques enhances the signal-to-background ratio by a factor of 4.5, leading to 9:1. To reach a similar level, the background acceptance of ν_eCC is required to be at least below 0.06% level. A tiny background leakage can be devastating for the ν_eCC selection.

The development of the ν_eCC selection happens in two stages. The first stage is the development of cut-based background taggers, which are again based on hand scans of background events. This effort suffers from the limited learning rate of a human being. About O(1000) events were examined in a two month time scale. Figure 17 (left) shows the signal-to-background ratio after applying background tagger cuts. While the resulting signal-to-background ratio is not satisfactory, the main motivation of this work to extract various features (i.e. variables) that can be used to reject backgrounds is achieved. The second stage of the development is to apply machine learning techniques, particularly BDTs with large statistics of Monte Carlo samples. Based on features (or variables) extracted during the first stage, a machine learning method based on BDTs is applied on large Monte Carlo events. The resulting ν_eCC selection is shown in Fig. 17 (right).
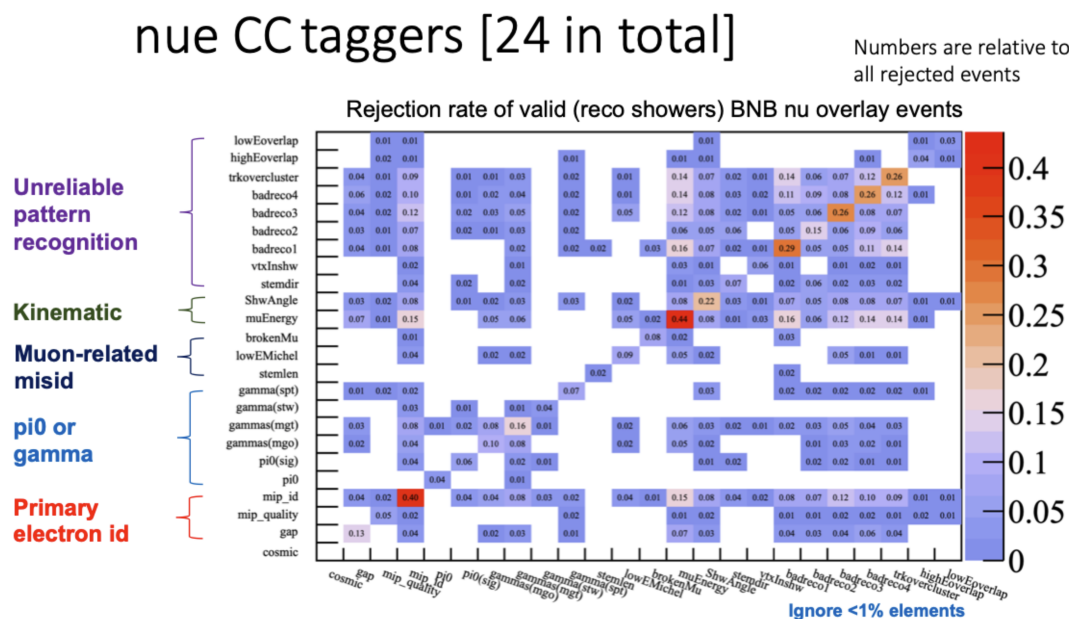

Figure 17: Cut-based (left in reconstructed visible energy) and an example of BDT-based (right in reconstructed neutrino energy) ν_eCC selections. Results in both plots are scaled to 5e19 POT. While the signal-to-background ratio is not good enough using hard cuts on background taggers, the extraction of features (or variables) build the foundation for applying BDTs.

The basic selection of inclusive ν_eCC events requires an EM shower with a reconstructed energy higher than ~60 MeV connecting to the primary neutrino vertex. The energy threshold is placed to exclude Michel electrons. When there are multiple reconstructed EM showers

connecting to the neutrino vertex, the EM shower with the highest energy is passed to the background tagger for further examination. Background taggers were developed by extracting features from a hand-scan effort. Figure 18 shows the rejection matrix of these background taggers. There are roughly five groups of background taggers. The first group focuses on the primary electron identification, including the examination of dQ/dx at the beginning (stem) of the shower and the identification of a gap between the shower and the neutrino vertex. The second group focuses on cases with multiple EM showers (e.g. π^0). The third group focuses on cases of muon-related misidentification. The fourth group focuses on background rejection with kinematics information (e.g. energy comparison between electron candidate and muon candidate, energy and angle of electron candidate, etc.). The last group focuses on the situation of unreliable pattern recognition. Note that there are many different failure modes for incorrect pattern recognition. Each failure mode would require a dedicated background tagger.
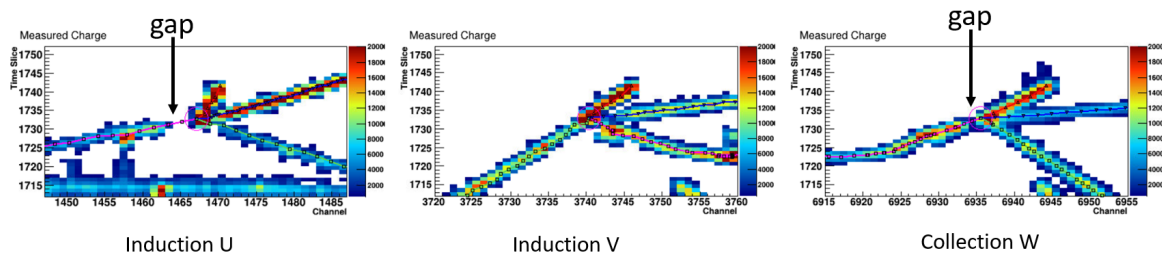

Figure 18: Rejection matrix of various background taggers. The diagonal term shows the amount of background events rejected by the selected background tagger. The off-diagonal term shows the amount of background events simultaneously rejected by two background taggers.

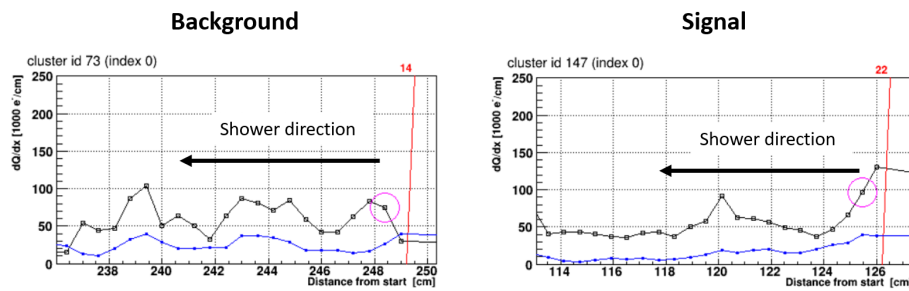The primary electron identification includes:

- Gap cut: the beginning of the EM shower in each 2D projection view is examined to search for a gap. Figure 19 shows an example.

- MIP quality cut to remove backgrounds: the beginning of the shower is examined to

ensure the quality of the shower stem. The checks include examinations of i) potential track overlap at the beginning of EM shower, ii) possible track splitting at the beginning of EM shower (i.e. the pair produced electron and positron are split instead of traveling in the same direction).

- MIP dQ/dx cut: we examine the dQ/dx at the beginning of the EM shower to ensure a MIP (electron-like) event. Instead of a likelihood approach, we calculate the length of MIP below a MIP threshold cut (i.e. 1.3 times of a MIP dQ/dx). The calculation of the length also considers the possibility of delta ray (i.e. a single sample with high dQ/dx). In addition, the high dQ/dx at the vertex must be taken into account. Figure 20 shows a signal and a background event.
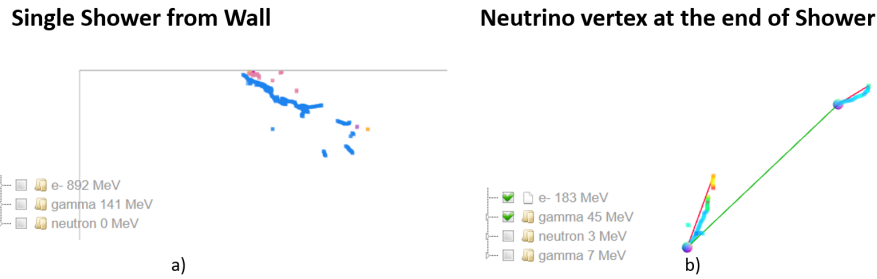

Figure 19: Illustration of gap identification for an EM shower.

Figure 20: Illustration of MIP identification for EM showers. (Left) A background event. The MIP dQ/dx is expected to be around 45k electrons/cm. (Right) A signal event with a high dQ/dx at the neutrino interaction vertex. The blue lines give a measure of the fit quality. The red line with a number is used to separate the different track segments. The identified neutrino vertices happen to be at larger distance from the start for these two examples.
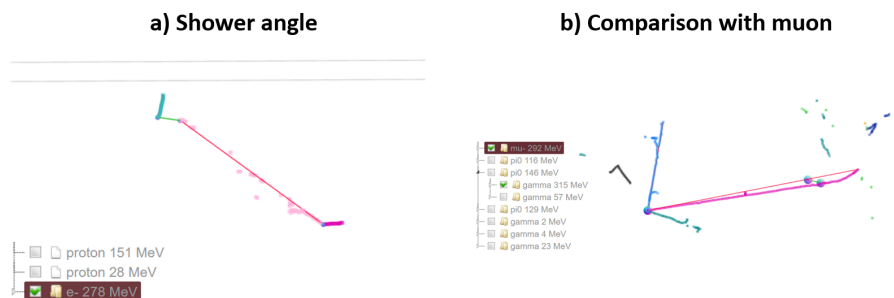
Figure 21 shows examples of gamma backgrounds from π^0 decay. Figure 22 shows examples of muon-related backgrounds. Figure 23 shows examples of backgrounds that can be rejected by kinematics information. Figure 24 and Fig. 25 shows the examples of backgrounds because of unreliable pattern recognition.

Single Shower from Wall   **Neutrino vertex at the end of Shower**
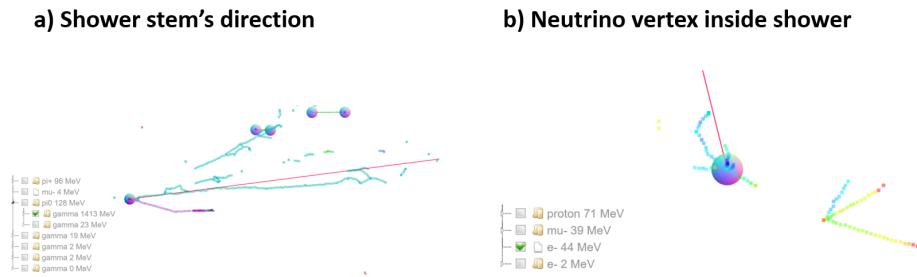

Figure 21: Illustration of single EM showers. (Left) An EM shower close to the top of the detector. (Right) The neutrino vertex is misidentified to be at the end of EM shower. The grey box represents the MicroBooNE active TPC volume, which is 2.56 m in the drift direction (X), 2.3 m high (Y), and 10.56 m along the beam axis (Z).

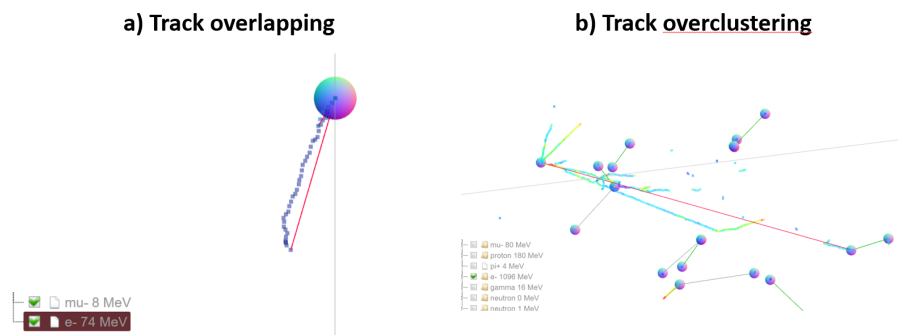**a) Long Shower stem**   **b) Broken Muon**

Figure 22: (Left) The identified EM shower has a long stem, which indicates an over-clustering situation (e.g. with a muon). (Right) A long muon is broken into pieces, which leads to a misidentification. The grey box represents the MicroBooNE active TPC volume, which is 2.56 m in the drift direction (X), 2.3 m high (Y), and 10.56 m along the beam axis (Z).

a) Shower angle   **b) Comparison with muon**

Figure 23: (Left) An EM shower going backward with respect to the neutrino beam direction. (Right) A long muon is found in addition to the electron candidate. The grey box represents the MicroBooNE active TPC volume, which is 2.56 m in the drift direction (X), 2.3 m high (Y), and 10.56 m along the beam axis (Z).

a) Shower stem's direction   **b) Neutrino vertex inside shower**

Figure 24: (Left) An example event where the shower stem's direction is not consistent with the shower's direction indicating an overclustering situation. (Right) The neutrino vertex is identified inside an EM shower.

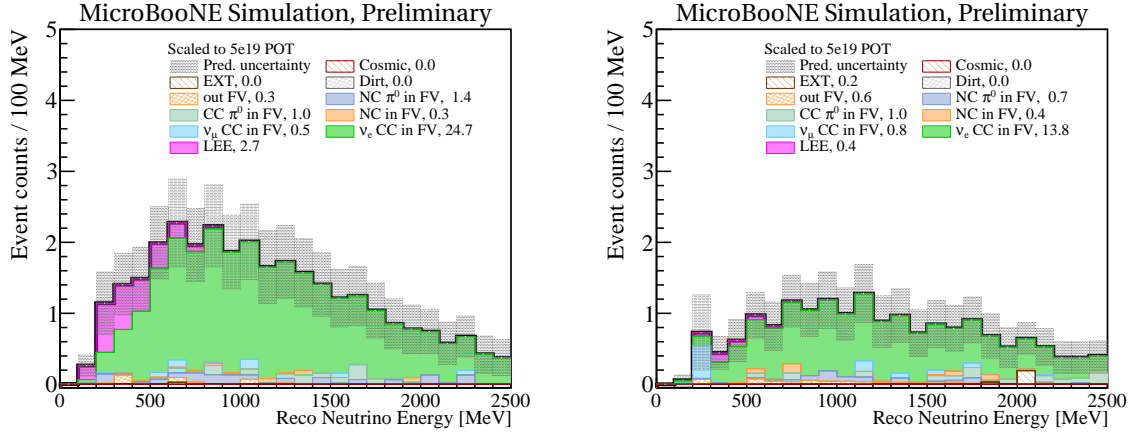**a) Track overlapping**   **b) Track overclustering**

Figure 25: (Left) An overlapping situation at the beginning of EM shower's stem region. (Right) An example of track overclustering situation. One of the tracks clearly shows the Bragg's peak. The grey box represents the MicroBooNE active TPC volume, which is 2.56 m in the drift direction (X), 2.3 m high (Y), and 10.56 m along the beam axis (Z).

With the human-engineered features selected, we apply BDT techniques to high-statistics Monte Carlo simulation samples to finalize the ν_eCC selection. The usage of machine learning techniques mitigates the limitation of human learning when processing large amount of events. From among different machine learning tools, the BDT technique is chosen because it is more robust and approachable for general users. The BDT package XGBoost [19], which provides fast and robust training through a parallel tree boosting, is used. XGBoost also improves the model generalization and overcomes the issues of overfitting in gradient boosting, enabling the use of a large pool of variables in the model.
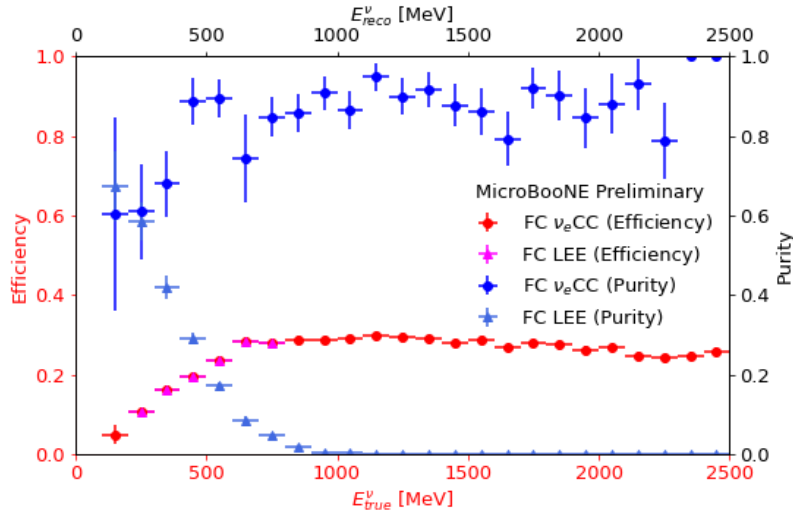
This BDT model achieves 83% nueCC purity (without LEE) and 42% efficiency combining both fully contained and partially contained events. Scaled to 5E+19 POT, we expect 39 nueCC events and 3.1 LEE events ($LEEx = 1$ hypothesis). The selected LEE signals are mostly fully contained nueCC events with energy less than 800 MeV. Figure 26 shows the energy spectra

for fully contained events and partially contained events. The 200 - 300 MeV peak in the partially contained figure is understood and due to a ν_μCC event with a large GENIE weight (8.9).

Figure 26: ν_eCC BDT selection at 5e19 POT. Left: fully contained events. Right: partially contained events. The gray area represents the total uncertainty of Monte-Carlo prediction, which includes statistical, cross section, and flux uncertainties (see Sec. 5).

The efficiency and purity for fully contained intrinsic nueCC and LEE events are shown in Fig. 27. For fully contained nueCC events, the overall selection efficiency and purity of intrinsic nueCC (without LEE) events are 26% and 86%, respectively. The efficiency of LEE signals is about 17%.
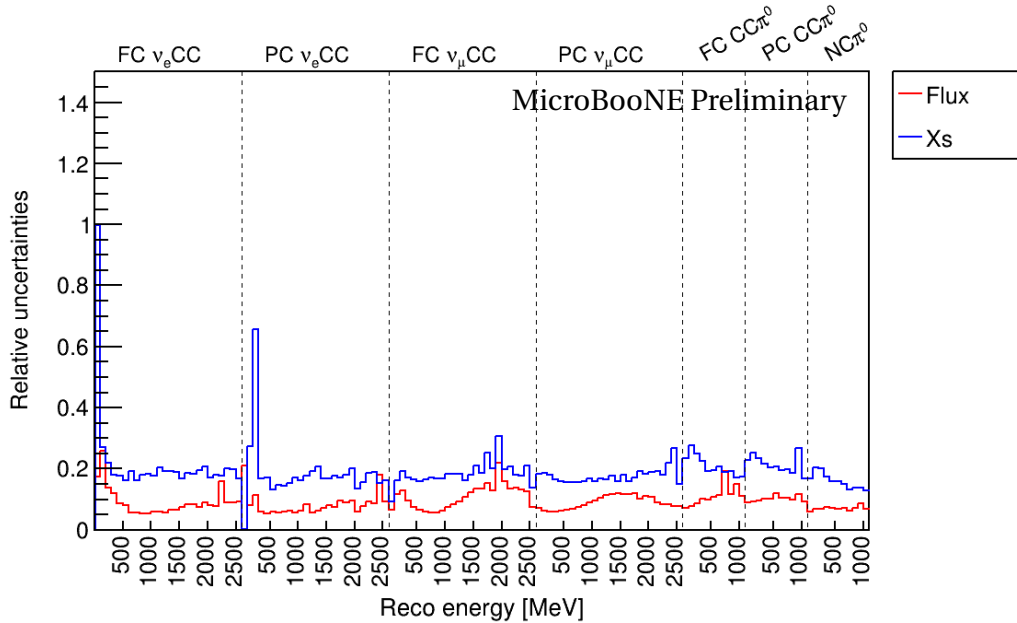

Figure 27: Efficiency and purity of selected fully contained nueCC events. Efficiency is calculated as a function of true neutrino energy. Purity is calculated as a function of reco neutrino energy. "ν_eCC" and "LEE" have identical efficiencies in the LEE region. "ν_eCC" purity does not consider "LEE" signals, while "LEE" purity considers 'ν_eCC' signals as background.
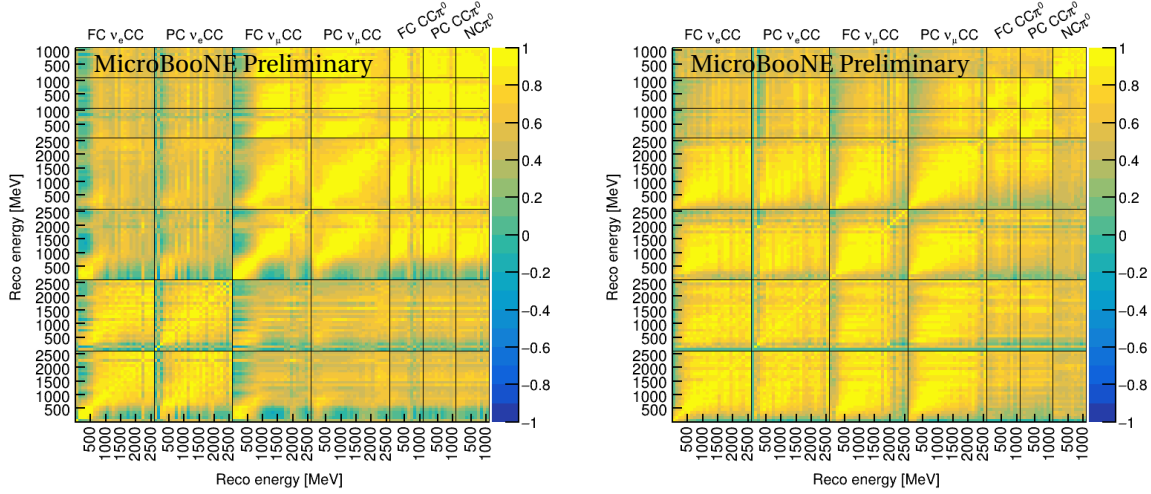
5 SYSTEMATIC UNCERTAINTIES

There are in total four sources of systematic uncertainties considered in this analysis. They are i) uncertainties because of the limited Monte Carlo statistics, ii) uncertainties from neutrino flux, iii) uncertainties from the neutrino-argon interaction cross section, and iv) additional uncertainties on the DIRT contributions. Because the Monte Carlo statistics for the detector-variation samples are currently limited, the detector effects are not included in the plots in this public note.

The estimation of uncertainties because of the limited Monte Carlo statistics is performed based on a Bayesian approach [20]. The details regarding the model of neutrino flux and neutrino-argon interaction cross sections (Xs) can be found in Ref. [5] and Ref. [6], respectively. These uncertainties impact the event distribution through both the normalization of distributions and the reconstruction of kinematics variable. The associated uncertainties are estimated using the common reweighting tools (flux [21] and Xs [22]). Two additional tuning parameters focusing the second-class currents that contribute to ν_e/ν_μCC cross section differences are added (Xs). The uncertainty associated with the beam flux (flux) is based on previous work in MiniBooNE [23]. An additional type of systematic uncertainties is related to hadrons interacting with external argon nuclei, which is estimated using GEANT4 by varying hadron's interaction cross sections with argon nuclei [24].

Figure 28: Relative uncertainties ($\frac{\text{absolute error}}{\text{central value}}$) of flux and cross section systematics for the seven channels.

Figure 28 shows the relative uncertainties of flux and cross section systematics for the seven channels. The information regarding the binning can be found in Sec. 6. The spikes (at 100 MeV of FC ν_eCC, 300 MeV of PC ν_eCC, and 2000 MeV of FC ν_μCC) of the cross section systematics are because of the low statistics, particularly of background, in the simulation. Left panel of Fig. 29 shows the correlations of flux systematics for the seven channels. There are strong correlations between i) ν_e low energy range and ν_μ low energy range, ii) ν_e high energy range and ν_μ high energy range, iii) ν_e high energy range and π^0s entire energy range. Right panel of Fig. 29 shows the correlations of cross section systematics for the seven channels. There are strong correlations between ν_e and ν_μ in the entire energy range.
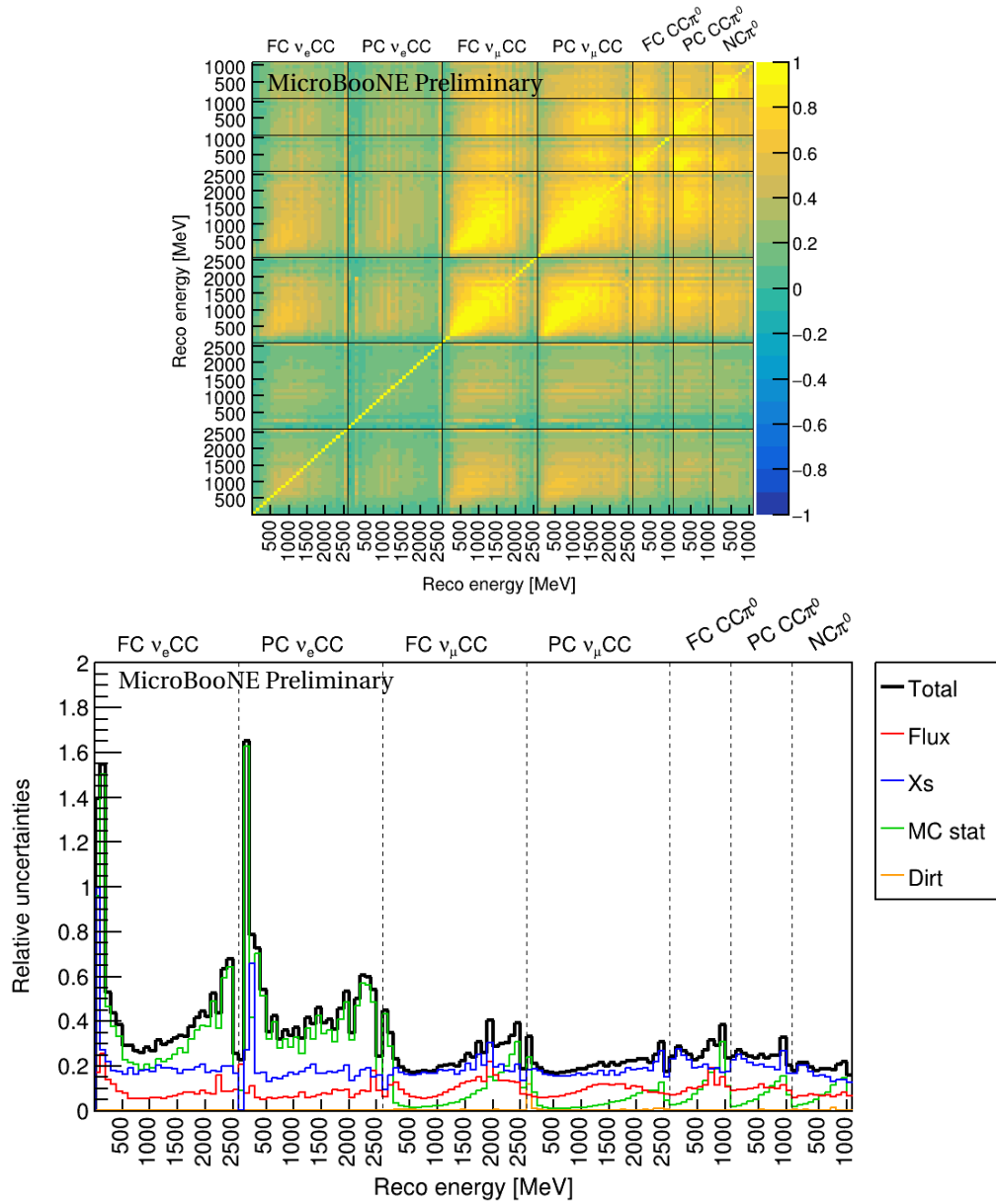

Figure 29: (Left) Correlations of flux systematics for the seven channels. (Right) Correlations of cross section systematics for the seven channels.

The DIRT events are neutrino interactions originated from outside the cryostat. The biggest uncertainty associated with the DIRT events are the modeling of the outside materials. In addition to the systematic uncertainties associated with flux/Xs, we assign an conservative relative 50% bin-to-bin (uncorrelated) uncertainty to DIRT events.

Top panel of Fig. 30 shows correlations of total systematic uncertainties for the seven channels. Bottom panel of Fig. 30 summarizes the relative uncertainties of total systematics for the seven channels. For ν_eCC channels, the estimation of backgrounds (i.e. EXTBNB and DIRT) suffers the most from the limited Monte Carlo statistics, given the predicted ν_eCC backgrounds from these samples are mostly zero.

Figure 30: (Top) Correlations of total systematics for the seven channels. (Bottom) Summary of relative uncertainties ($\frac{\text{absolute error}}{\text{central value}}$) of total systematics for the seven channels.

6 ANALYSIS OF BNB OPEN DATA AT 5.3E19 POT

Before proceeding to the full eLEE analysis, validation on neutrino energy reconstruction is performed and shown in this section. Validation on event selection using NuMI data is presented in Sec. 7, e.g. the ν_e BDT score distribution in Fig. 54.

As discussed in Sec. 2.1, three methods are used to reconstruct the neutrino energy: i)

travel range, ii) recombination model by converting dQ/dx to dE/dx, and iii) EM shower energy reconstruction based on the ionization charge. The simulation of the travel range for various particle relies on GEANT4 simulation. The recombination model used to convert dQ/dx to dE/dx is taken from Ref. [9]. A dedicated validation was done by comparing reconstructed dQ/dx as a function of the residual range between data and simulation in Fig. 31. While a difference is observed between the data and the simulation central value, the agreement is clearly improved between data and the detector variation sample ("Recomb2"), which is used to estimate the detector-related systematics.

For the EM shower energy reconstruction, the best validation is from the comparison of the reconstructed π^0 mass between simulation and data. Figure 32 shows the consistency between the data and simulation in all three π^0 channels. For the π^0 kinetic energy, only the EM shower energy reconstruction is involved. For the 7-channel fit, we measure the FC ν_eCC, PC ν_eCC, FC ν_μCC, and PC ν_μCC channels using reconstructed neutrino energy as described in Sec. 2.1. We chose to use 100 MeV bins from 0 to 2500 MeV, plus the overflow bin for 26 bins in total. For the FC CCπ^0, PC CCπ^0, and NCπ^0 selections, we use the kinetic energy of the π^0 after constraining the π^0 mass (M_{π^0}):

$$T_{\pi^0} = M_{\pi^0} \times \left(\sqrt{\frac{2}{\left(1 - \alpha^2\right) \cdot (1 - \cos\theta)}} - 1 \right), \tag{1}$$

with asymmetry of the gamma energies: $\alpha = \left(E_{\gamma\,1} - E_{\gamma\,2}\right) / \left(E_{\gamma\,1} + E_{\gamma\,2}\right)$ and angle between the two gammas in the lab frame θ. We chose to use 100 MeV/c^2 bins from 0 to 1000 MeV/c^2, plus the overflow bin for 11 bins in total. For the π^0 channels, we chose the π^0 kinetic energy instead of the reconstructed neutrino energy, since it is expected to better reflect the uncertainties in π^0 production cross section, therefore is expected to provide a better constraint to backgrounds of ν_eCC event selection.
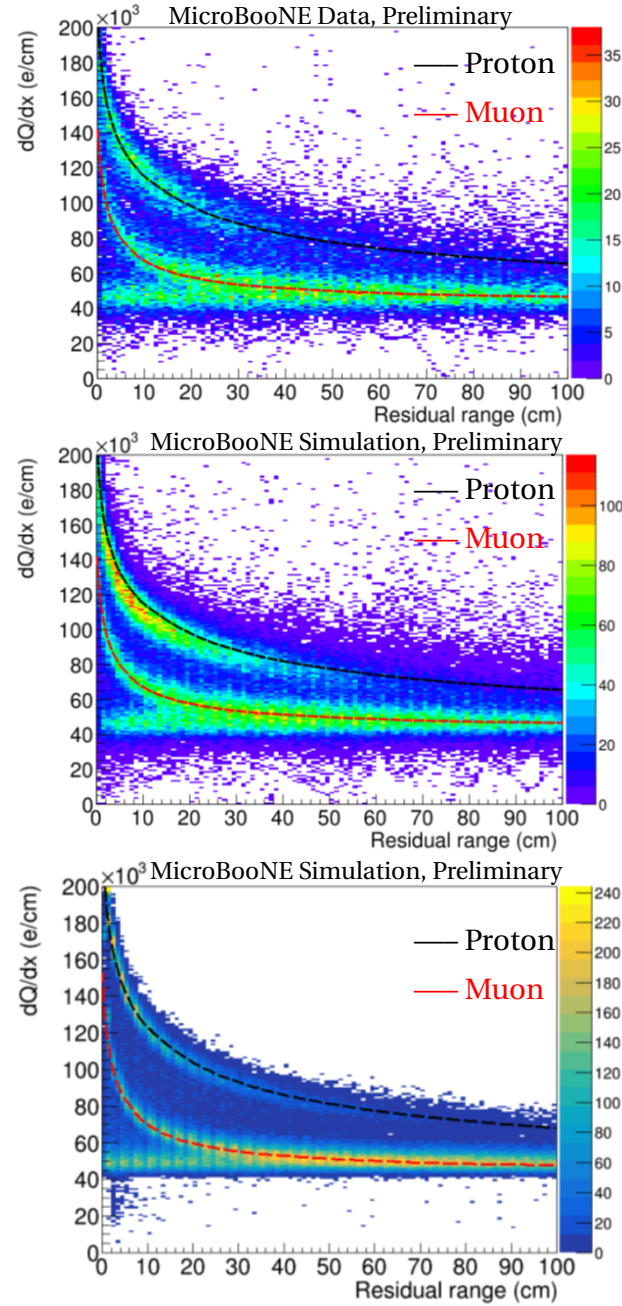
We adopted the covariance matrix formalism to construct the χ^2 test statistics:

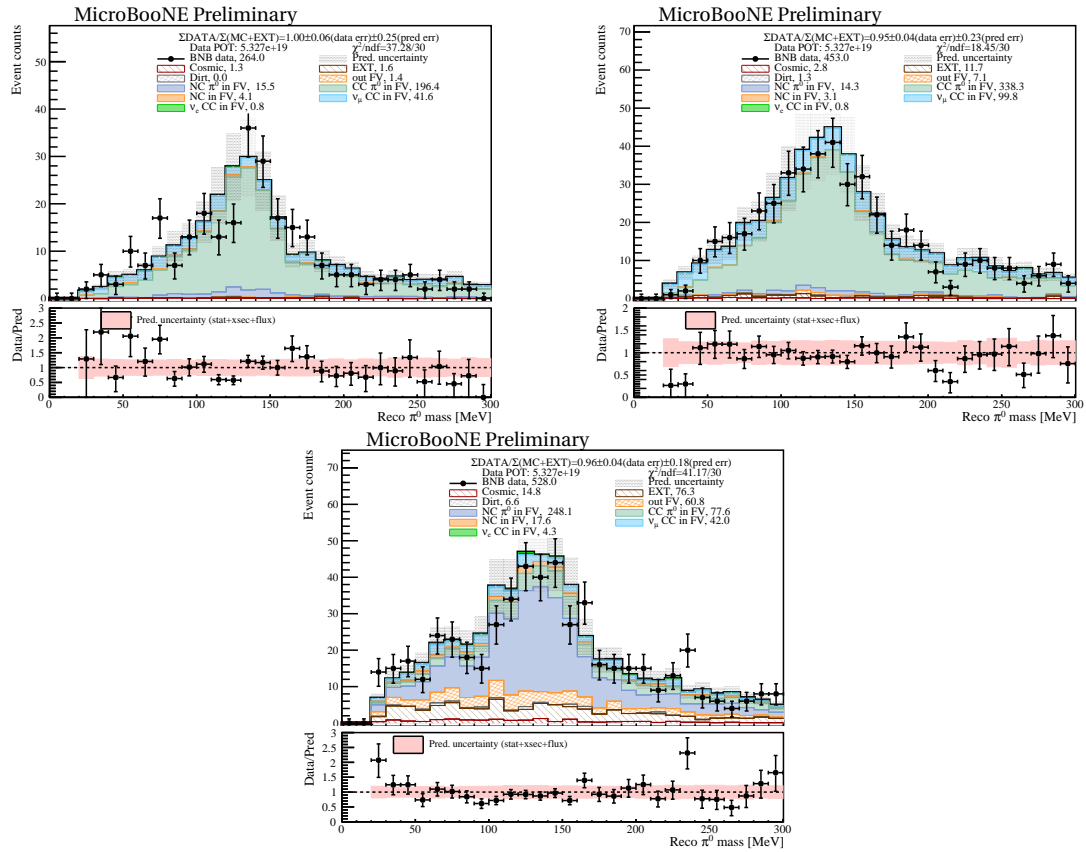$$\chi^2 = (M - P)^T \times Cov_{full}^{-1}(M, P) \times (M - P), \tag{2}$$

where M and P are vectors of measurement and prediction, respectively. For the 7-channel fit, the length of M (also P) is 137 = 26×4 + 11×3. The $Cov(M, P)$ is the full covariance matrix:

$$Cov = Cov_{CNP}^{stat} + Cov_{MC}^{stat} + R^T \times \left(Cov_{xs}^{sys} + Cov_{flux}^{sys} + Cov_{det}^{sys} + Cov_{add}^{sys} \right) \times R, \tag{3}$$

where Cov_{CNP}^{stat} is the diagonal covariance matrix constructed based on the combined-Neyman-Pearson (CNP) method [25] with the statistical uncertainty square being $3/(1/M_i + 2/P_i)$ for

Figure 31: Comparison of data and simulation for the dQ/dx as a function of residual range: (top) data, (middle) simulation central value, and (bottom) simulation with "recomb2" detector variation. The black and red dashed lines are representing the predictions of the recombination model for protons and muons, respectively. They are the same in all three plots.
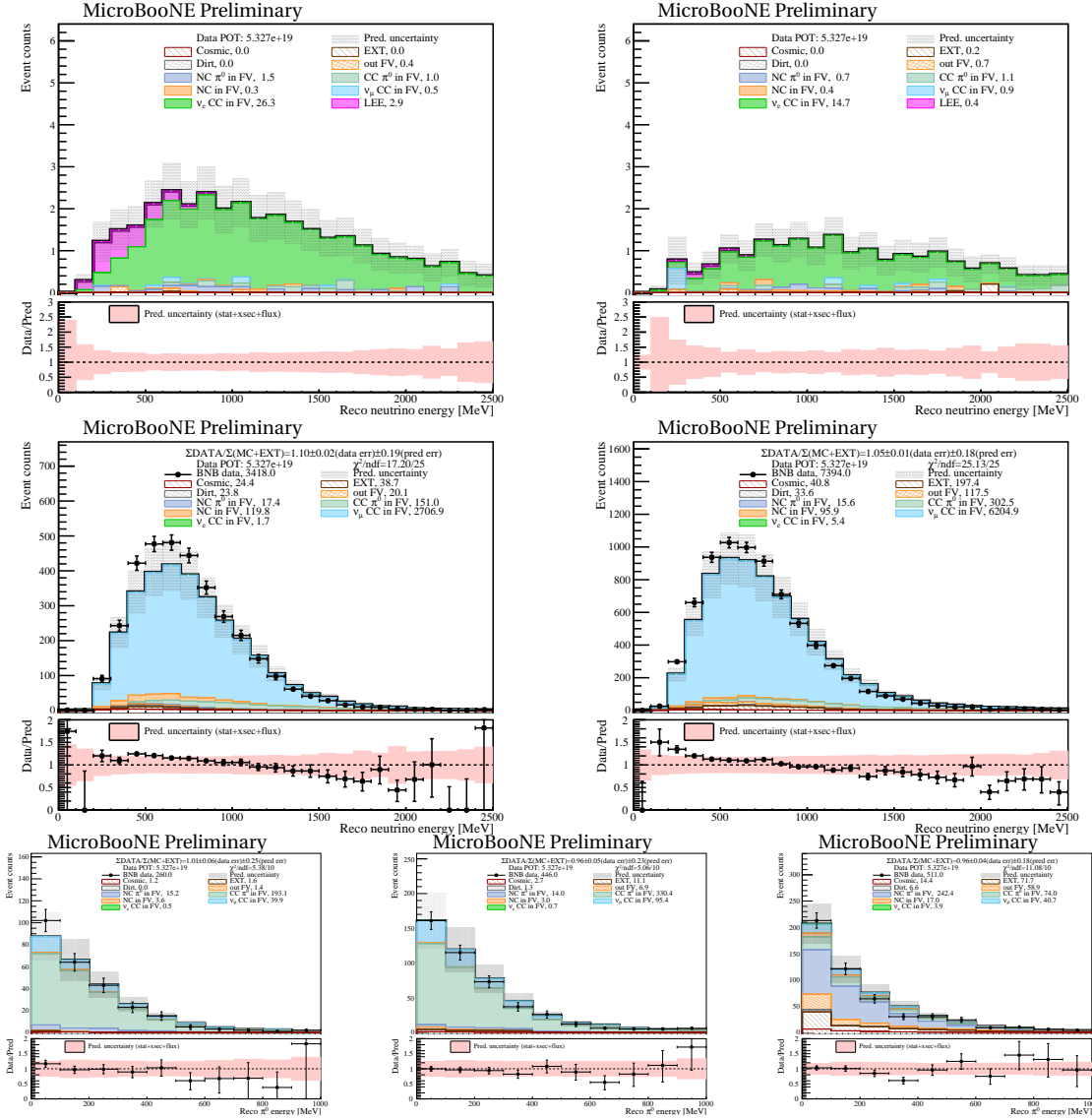
Figure 32: Comparison of the reconstructed π^0 mass between data and simulation with only statistical uncertainties: (top left) FC CCπ^0, (top right) PC CCπ^0, and (bottom) NCπ^0. A consistency is observed between the data and simulation validating the energy scale reconstruction for EM shower.

the ith bin. The Cov_{MC}^{stat} is the diagonal covariance matrix containing the statistical uncertainties corresponding to finite statistics from Monte Carlo simulations. The other four covariance matrices Cov_{xs}^{sys}, Cov_{flux}^{sys}, Cov_{det}^{sys}, Cov_{add}^{sys}, are the covariance matrices corresponding to uncertainties from cross section, neutrino flux, detector performance, and DIRT, respectively. The dimensions of these four covariance matrices are bigger than the final covariance matrix. There are i) FC LEE ν_eCC (26 bins), ii) PC LEE ν_eCC (26 bins), iii) nominal 7-channels excluding the contribution of EXTBNB (137 bins), and iv) 7-channels from EXTBNB (another 137 bins). Here, the two LEE ν_eCC channels are separated out from the intrinsic ν_eCC channels, since the LEE strength is expected to change. In addition, the EXTBNB contributions to the 7 channels are also separated out, since they are not subject to various systematics (i.e. direct background measurements). R is a matrix collapsing the full covariance matrix (dimension of $26 + 26 + 137 + 137 = 326$) to the final covariance matrix (dimension of 137). LEE ν_e channels are added to the corresponding ν_eCC channels. EXTBNB background contributions are also added to the corresponding channels. Except for Cov_{add}^{sys}, all covariance matrices depend on the LEE strength x.[]

Given the χ^2 definition in the previous section, we can perform the goodness-of-fit test. Following the recommendation of Ref. [26], we adopt the Pearson chisquare construction (instead of the CNP construction) for the statistical term for data:

$$Cov = Cov_{Pearson}^{stat} + Cov_{MC}^{stat} + R^T \times \left(Cov_{xs}^{sys} + Cov_{flux}^{sys} + Cov_{det}^{sys} + Cov_{add}^{sys} \right) \times R, \qquad (4)$$

with the statistical uncertainty being the square root of P_i for the ith bin. Given the null hypothesis (i.e. standard model), the chisquare value can be used to perform the goodness-of-fit test by comparing with the chisquare distribution with 137 degrees of freedom (dof), which is the total number of bins in the 7-channel analysis. In this technote, the detector systematic uncertainties are not included in the plots and results because of the limited statistics of the MC samples with varied detector effects.

Figure 33: Distribution of 7-channel selection results from open data assuming $LEEx = 1$: (from left to right, top to bottom) fully contained ν_e CC, partially contained ν_e CC, fully contained ν_μ CC, partially contained ν_μ CC, fully contained CC π^0, partially contained CC π^0, and NC π^0. The available open data result is overlaid and the pink band in the bottom panel presents the systematic uncertainty of the prediction, including MC statistic, cross section and flux uncertainties.

The above goodness-of-fit test provides an overall evaluation of the model and the null hypothesis compatibility with the data. This evaluation can be zoomed into different parts of the model using the conditional covariance matrix formalism [27, 28]. For example, given the

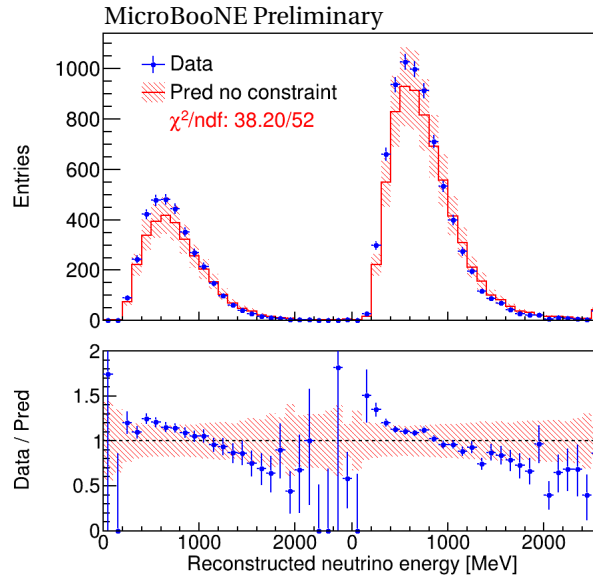full covariance (stat + sys) containing two channels (X, Y):

$$\Sigma = \begin{pmatrix} \Sigma^{XX} & \Sigma^{XY} \\ \Sigma^{YX} & \Sigma^{YY} \end{pmatrix}, \quad n : \text{measurement}, \quad \mu : \text{prediction}, \tag{5}$$

we can derive the prediction on X given the constraints on Y:

$$\mu^{X,constrained} \;\; = \;\; \mu^X + \Sigma^{XY} \cdot \left(\Sigma^{YY}\right)^{-1} \cdot \left(n^Y - \mu^Y\right), \tag{6}$$

$$\Sigma^{XX,constrained} \;\; = \;\; \Sigma^{XX} - \Sigma^{XY} \cdot \left(\Sigma^{YY}\right)^{-1} \cdot \Sigma^{YX}. \tag{7}$$
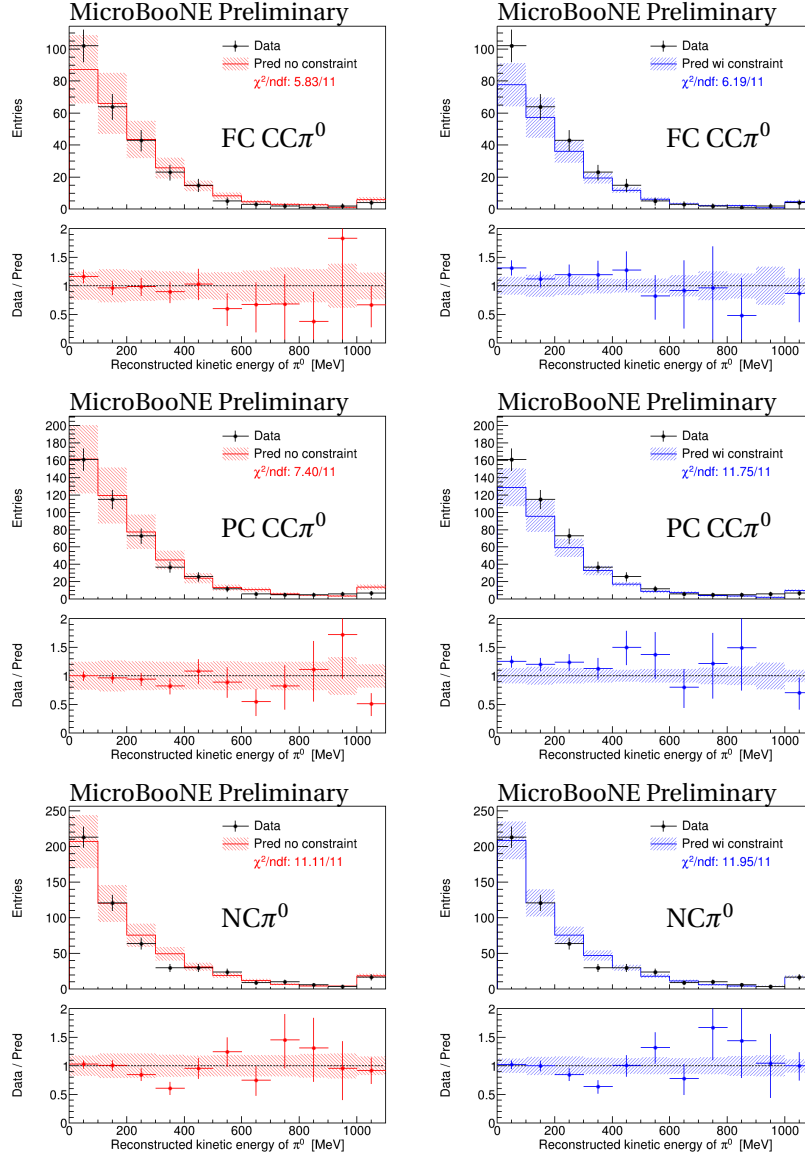
Thus, a goodness-of-fit test can be performed on Y first, and then performed on X after the constraints of Y. This allows the examination of the model compatibility with X and Y individually.

Figure 34: Comparison between data and prediction for ν_μCC channels. The first (second) 26 bins represent the FC (PC) channel. The error band represents the total systematic uncertainty from MC statistic, cross section, and flux. The bin index represents the bin number in reconstructed neutrino energy spanning from 0 to 2500 MeV at a bin width of 100 MeV. The 26th bin represents the overflow bin for reconstructed neutrino energy higher than 2500 MeV.
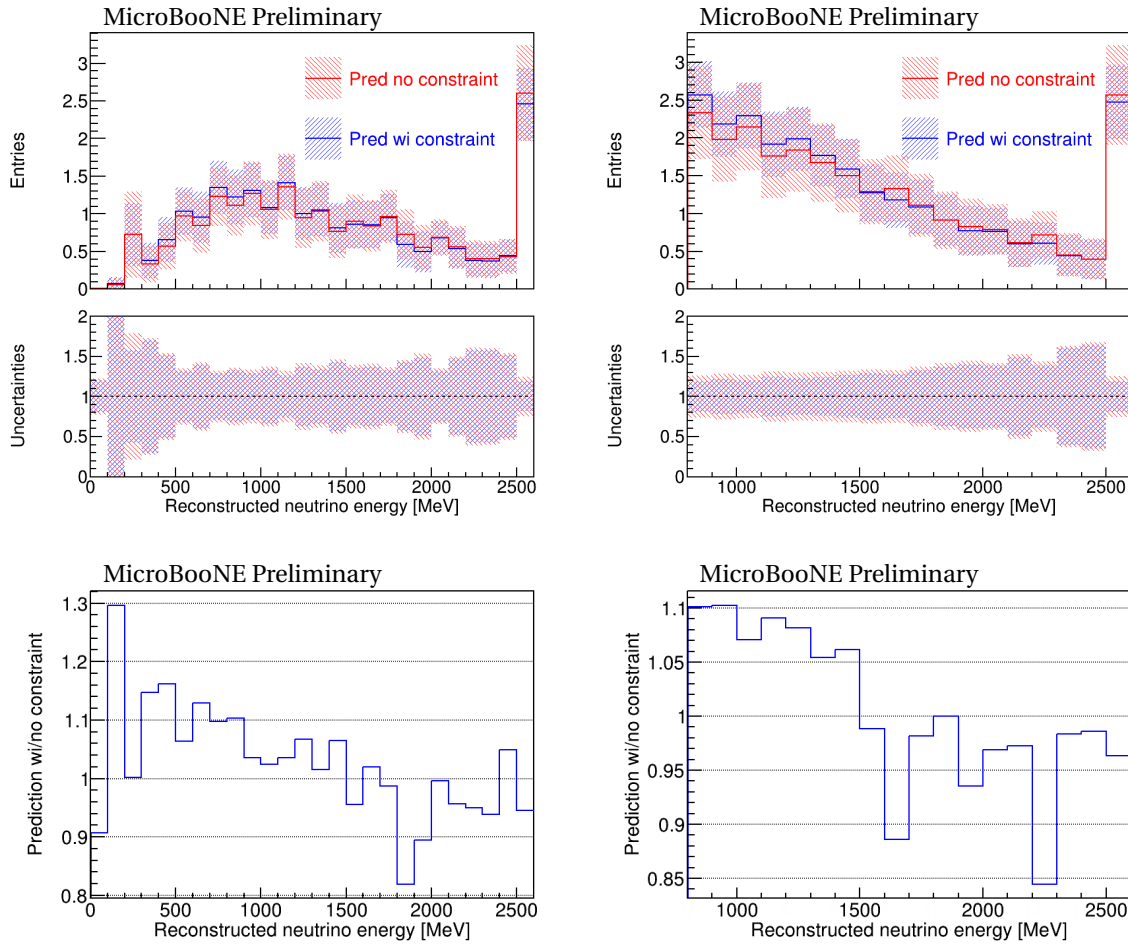
With the aforementioned techniques and selection criteria, the 7-channel selection results from open data are presented. Figure 33 shows the stacked histograms of each component of the signal and background events from MC prediction. Open data result is overlaid with all systematic uncertainties including Bayesian statistical uncertainty of MC prediction central

values, flux and cross section systematic uncertainties. Figure 34 shows the comparison between data and prediction with the current systematic uncertainties. At low (high) energies, the data is higher (lower) compared to the central values of the Monte-Carlo prediction. The goodness-of-fit combining both ν_μCC channels is $\chi^2/NDF = 38.20/52$, which indicates the data/MC differences is within the current systematic uncertainties. In comparison, the χ^2/NDF is $227.34/52$ when the systematic uncertainties are excluded.

Figure 35: Comparison between data and prediction for three π^0 channels: (top) FC CCπ^0, (middle) PC CCπ^0, (bottom) NCπ^0. Left (right) panels show the result before (after) applying the ν_μCC constraints. The error band shows the total systematic uncertainty from MC statistic, cross section, and flux. The bin index represents the bin number in the reconstructed kinetic energy of π^0 from 0 to 1000 MeV at a bin width of 100 MeV. The 11th bin represents the overflow bin.

Figure 35 shows the three π^0 channels before and after applying constraints from the ν_μCC channels. After applying constraints, the prediction of CCπ^0 channels is reduced, which can be explained by the deficit in ν_μCC at high energies. The GoF of all tests are very good, indicating the difference between the data and predictions are well within the total statistical and systematic uncertainties. The GoF after applying constraints are slightly worse than those before applying constraints, which is the result of reduced uncertainties and (in some cases) larger difference between data and prediction.
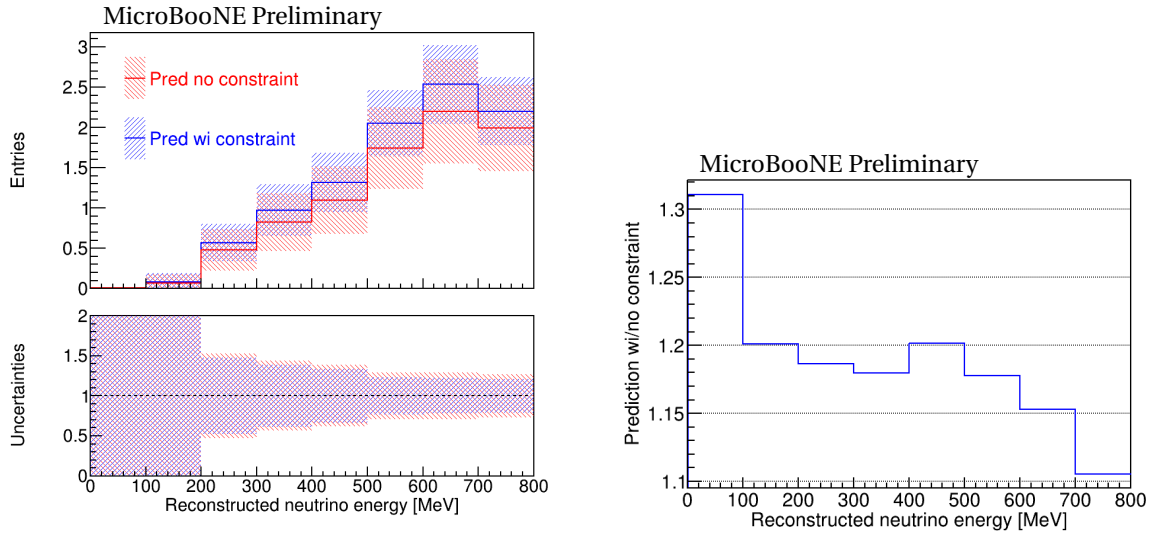

Figure 36: Comparison of prediction for PC ν_eCC (left) and high-energy FC ν_eCC (right) before and after applying constraints from ν_μCC and π^0 channels. The error bands in the top panels show the total systematic uncertainty from MC statistic, cross section, and flux. The bottom panels show the ratio of prediction after applying constraints to that before applying constraints. For the PC ν_eCC channel (left), the bin index represents the bin number in the reconstructed neutrino energy from 0 to 2500 MeV with a bin width of 100 MeV. The last bin is the overflow bin. For the high-energy FC ν_eCC channel (right), the bin index represents the bin number in the reconstructed neutrino energy from 800 MeV to 2500 MeV with a bin width of 100 MeV. The last bin is the overflow bin.

Figure 36 shows the two ν_eCC side-band channels (partially contained events, and fully contained high energy events > 800 MeV) after applying constraints from the ν_μCC and π^0 channels. The prediction after applying constraints is systematically higher (lower) in the low (high) energy region, which is the direct result of an excess (deficit) of events in the ν_μCC channel at low (high) energy.

Figure 37 shows the low-energy FC ν_eCC channel after applying constraints from all other channels. The prediction after applying constraints is systematically higher, which is the direct result of an excess of events in the ν_μCC channel at low energy. The enhanced prediction in FC ν_eCC in the low-energy region leads to improved sensitivity in the eLEE search.

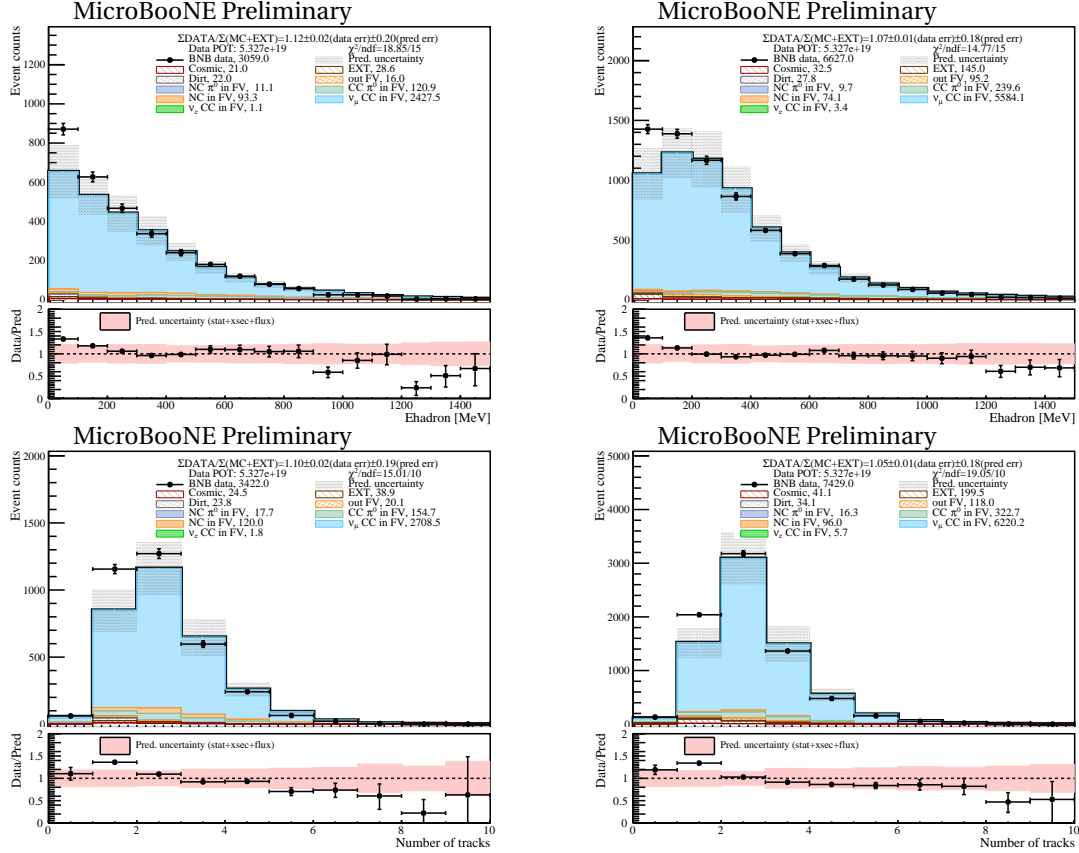
Figure 37: Comparison of prediction for the low-energy FC ν_eCC channel before and after applying constraints from all other channels. The error band in the left panel shows the total systematic uncertainty from MC statistic, cross section, and flux. The right panel show the ratio of prediction after applying constraints to that before applying constraints. The bin index represents the bin number of the reconstructed neutrino energy from 0 to 800 MeV with a bin width of 100 MeV.

6.1   Model Validations

In this section, we provide more validations with BNB ν_μCC candidates to demonstrate good agreement between data and Monte Carlo predictions within estimated systematic uncertainties. As shown in Fig. 34, there are some excess (deficit) in data with respect to central value Monte Carlo predictions at low (high) energy region. Evaluations are performed to examine the data/MC comparison in neutrino vertex positions as well as the primary muon energy and angles. The hypothesis that the excess ν_μCC events at low-energy region
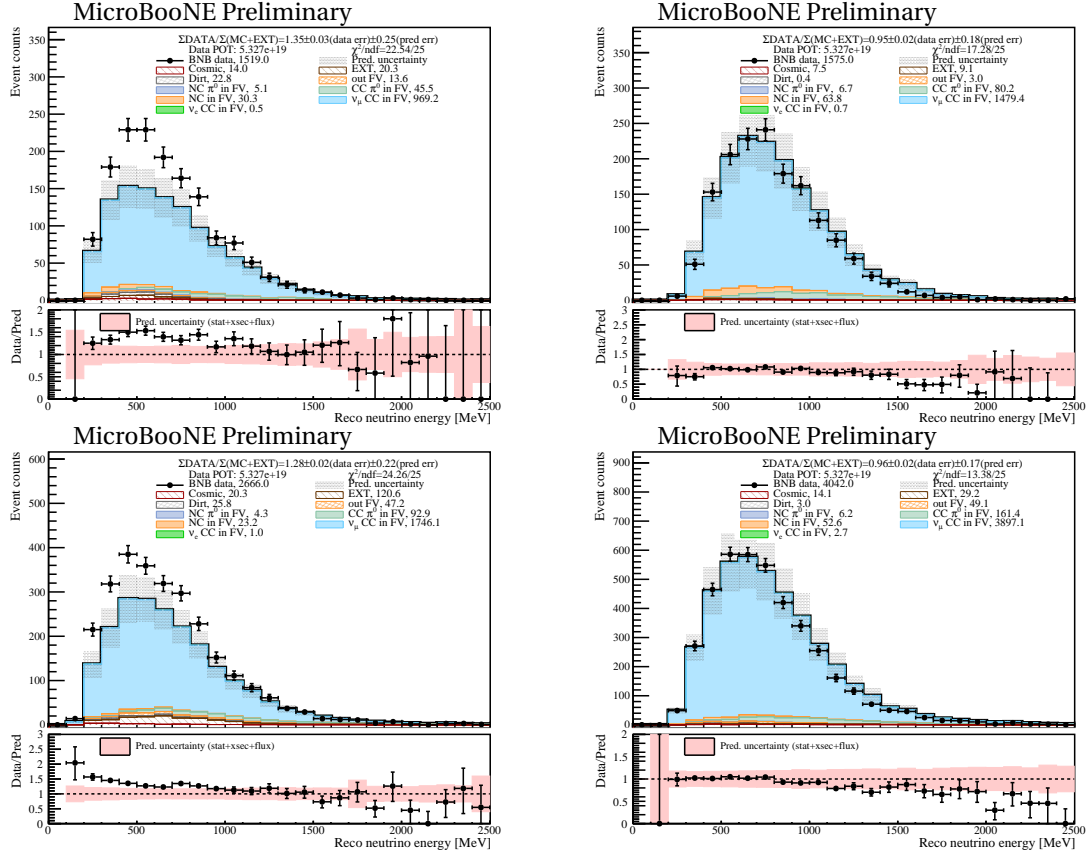
are the result of bad reconstruction or excess cosmic-ray backgrounds is rejected.

Figure 38: (Top) Distribution of reconstructed hadronic energy (energy transfer/difference between reconstructed neutrino energy and primary muon energy) for ν_μ CC candidate events. (Bottom) Distribution of the number of track-like particles for ν_μ CC candidate events. Left: fully contained events. Right: partially contained events.
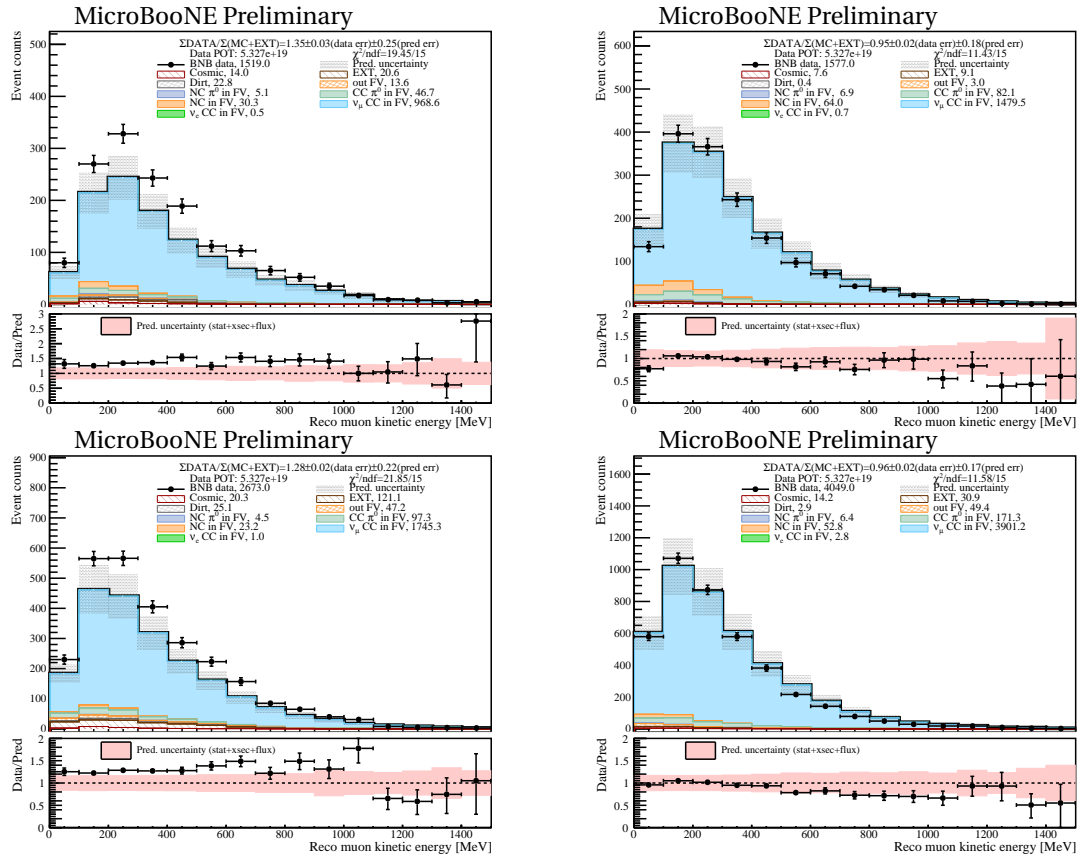
One hypothesis to explain the difference between data and central value Monte Carlo observed in Fig. 34 is a shift in the reconstructed neutrino energy, particularly because of the missing energy in the detection of the hadronic system. Top panel of Fig. 38 shows the reconstructed hadronic energy distribution for ν_μ CC candidate events. While an excess can be seen in low hadronic energy region, there is no clear shift in energy at high hadronic energy region. One potential explanation to this observation is that there might be some mechanism where the full energy transfer to Argon system is missing (e.g. by energetic neutrons). Later, we will use the conditional covariance matrix formalism to show that we can safely exclude such a hypothesis (see Sec. 6.2). Bottom panel of Fig. 38 confirms this observation which presents the number of track-like particles including primary muons, protons, or charged pions. A proton track requires a kinematic energy > 35 MeV, i.e. track length > 1cm, and a charged pion requiring kinematic energy > 10 MeV. The Pearson goodness-of-fit (GoF :

χ^2/ndf), which considers the bin-to-bin correlated (off-diagonal terms in covariance matrix) uncertainties, can be found in each plot. The GoF values are all quite reasonable indicating consistency between data and overall model prediction (with its uncertainties).
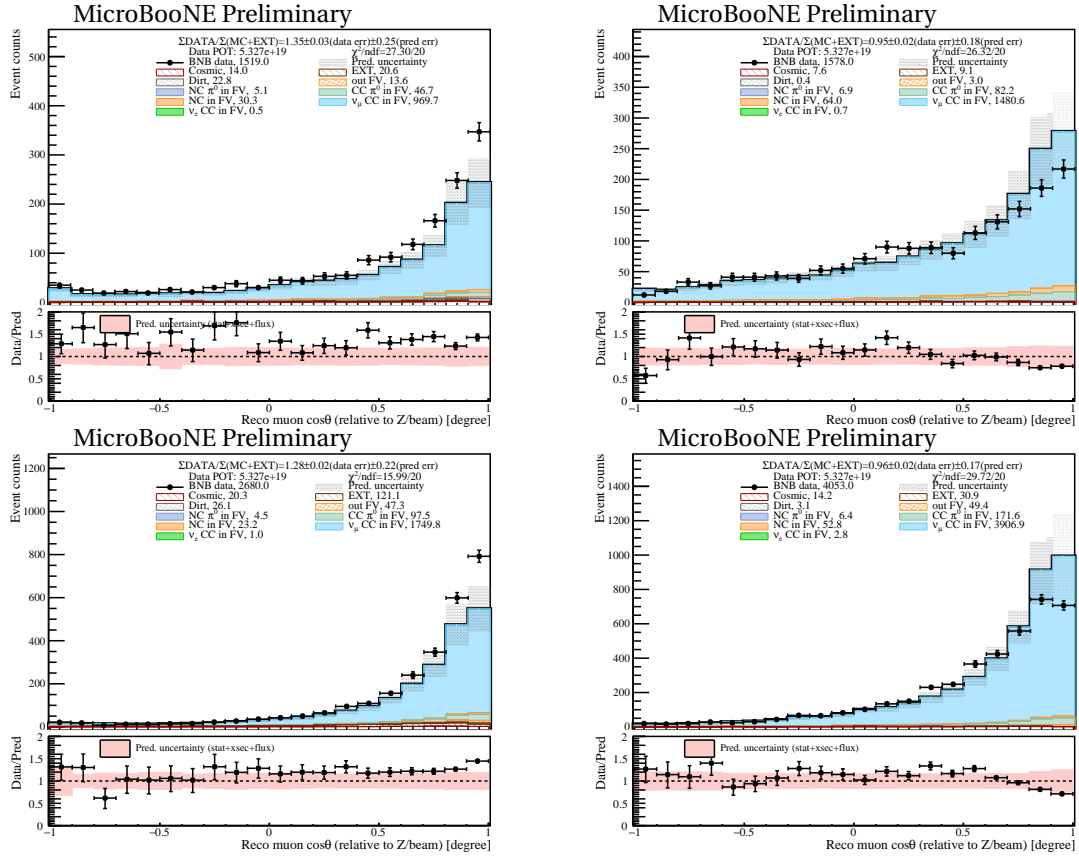

Figure 39: Distribution of reconstructed neutrino energy for ν_μ CC candidate events. Left: without protons. Right: with one or more protons. Top: fully contained events. Bottom: partially contained events.

Inspired by the excess in hadronic and track multiplicity plots, we divide the inclusive ν_μ CC candidate events into two different categories: events without protons (> 35 MeV) and with one or more protons. Number of protons is counted based on reconstructed information and includes both primary protons and isolated protons (e.g. from neutron scattering). Figure 39 shows the results after this categorization. $0p$ channel shows excess except for the very high energy region, and Np channel mainly shows deficit in very high energy region. This observation can safely exclude the hypothesis that the "slope" of the inclusive ν_μ CC data/MC ratio is attributed to any beam flux issues, which is further confirmed by the analysis of NuMI data in Sec. 7, or energy reconstruction of the primary muon.
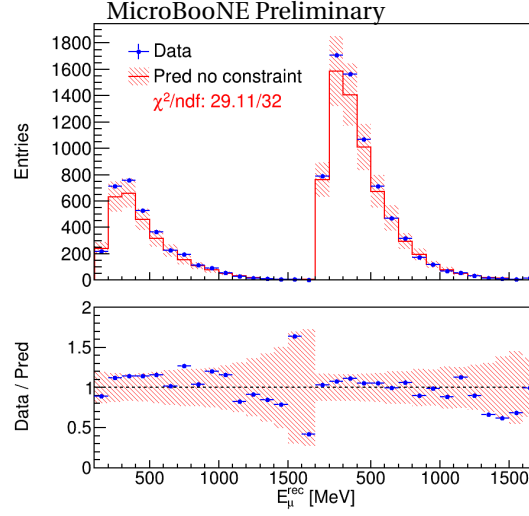
Figure 40: Distribution of reconstructed muon kinematic energy for ν_μ CC candidate events. Left: without protons. Right: with one or more protons. Top: fully contained events. Bottom: partially contained events.

The data/MC comparison in muon energy and angles are shown in Fig. 40 and Fig. 41, respectively. The hotspot of the excess or deficit in $0p$ or Np channels corresponds to forward-going muons. For the Np channels, the deficit in data for the most forward-going muons has also been observed in the MicroBooNE cross section measurements [29, 30, 31].
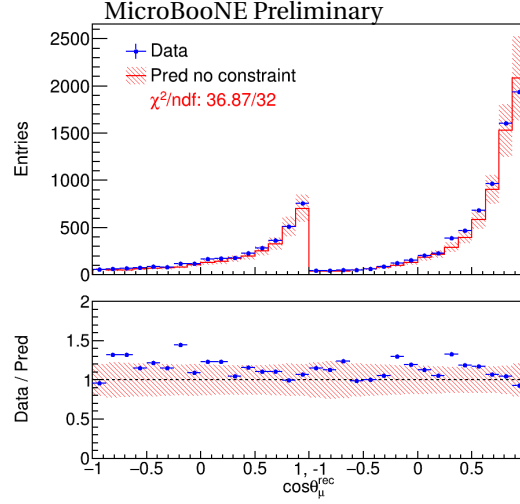
Figure 41: Distribution of cosθ of reconstructed muons for ν_μ CC candidate events. θ is the polar angle relative to the neutrino beam/incoming direction. Left: without protons. Right: with one or more protons. Top: fully contained events. Bottom: partially contained events.

Beside the general data/MC comparison, for eLEE search, another important validation is on the modeling of the conversion from true neutrino energy to the reconstructed neutrino energy. The systematic uncertainties without the detector systematics are dominated by the neutrino flux and cross section systematics. Figure 42 shows the comparison between data and prediction as a function of the reconstructed muon energy E_μ^{rec} for both fully contained (FC) and partially contained (PC) channels. Even without considering the detector systematics, the GoF (χ^2/NDF) is below unity in both cases showing good agreement between data and model prediction.
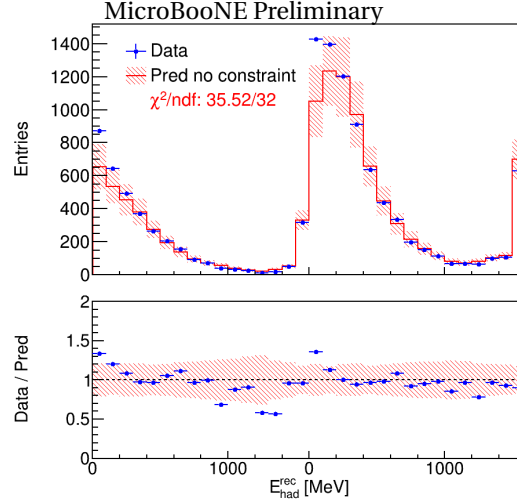
Figure 42: Comparison between data and prediction as a function of E_μ^{rec}: The statistical, cross section, and flux systematic uncertainties are included in the bands. The first 15 bins with 100 MeV per bin correspond to the fully contained events from 0.1 GeV to 1.6 GeV. The 16th bin is the overflow bin corresponding to fully contained events above 1.6 GeV. The next 15 bins with 100 MeV per bin correspond to the partially contained events from 0.1 GeV to 1.6 GeV. The last bin is the overflow bin corresponding to the partially contained events above 1.6 GeV.

Figure 43 shows the comparison between data and prediction as a function of the reconstructed muon angle $\cos\theta_\mu^{rec}$ for both fully contained (FC) and partially contained (PC) channels. The GoF is slightly above unity (p-value of 0.25) showing good agreement between data and model prediction. Note, at the forward angle $\cos\theta_\mu^{rec} \sim 1$, the data is higher than the model prediction in the FC sample, while the data is lower than the model prediction in the PC sample. This observation is consistent with the data excess in the $1\mu0p$ channel and the data deficit in the $1\mu Np$ channel. Since the percentage of $1\mu0p$ (or $1\mu Np$) is different between the FC and PC samples, the data has different behaviours in the forward muon angle bin with respect to the central value Monte Carlo prediction.

Figure 43: Comparison between data and prediction as a function of $\cos\theta_\mu^{rec}$ (relative to Z/beam). The statistical, cross section, and flux systematic uncertainties are included in the bands. The first 16 bins correspond to the fully contained events covering from -1 to 1. The next 16 bins correspond to the partially contained events covering from -1 to 1.

Figure 44 shows the comparison between data and prediction as a function of the reconstructed energy of the hadronic system E_{had}^{rec}. The GoF (without detector systematics) is slightly above unity (p-value of 0.31) showing good agreement between data and model prediction. We should further note that the data of the lowest E_{had}^{rec} bin is above the prediction and outside the uncertainty band. This difference is consistent with the fact that data are systematically higher than the prediction at $1\mu0p$ channel. Since the E_{had}^{rec} is low for these events, it is natural to raise the question whether the model describes the missing energy because of neutrons or low-energy gammas well. We will come back to this point and show the current model is sufficient in describing the observations in data with conditional covariance matrix in Sec. 6.2.

Figure 44: Comparison between data and prediction as a function of E_{had}^{rec}. The statistical, cross section, and flux uncertainties are included in the bands. The first 15 bins with 100 MeV per bin correspond to the fully contained events from 0 GeV to 1.5 GeV. The 16th bin is the overflow bin corresponding to fully contained events above 1.5 GeV. The next 15 bins with 100 MeV per bin correspond to the partially contained events from 0 GeV to 1.5 GeV. The last bin is the overflow bin corresponding to the partially contained events above 1.5 GeV.

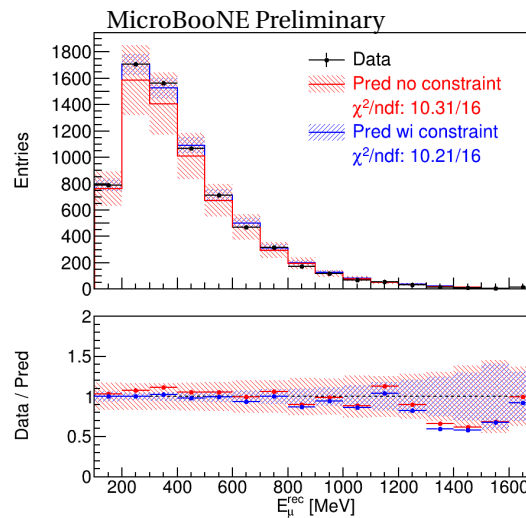## 6.2   Further Model Validations with Conditional Covariance Matrix

Using the conditional covariance matrix (introduced in Sec. 5), we demonstrate that the difference between the modeling of the missing energies (because of neutrons or low-energy gammas or activities outside TPC) and that in real data is within the quoted cross section systematic uncertainties.

For PC events, the reconstructed (neutrino, muon, hadronic) energy only takes into account the visible part of the system inside the active TPC volume. The conversion between the true energy and the reconstructed energy thus has stronger dependence on the overall model. Therefore, it is crucial to perform dedicated validations on the modeling of missing energy. Since the missing energy is invisible by definition, the validation can only be performed on the reconstructed energy. As shown in the previous section, the direct comparison of the PC distributions with the overall model yields good GoF values indicating consistent results. However, these tests include all sources of systematics, which may hide the potential discrepancies on the modeling of missing energy for the PC events. To validate the modeling of the missing energy for the PC events, we perform a more stringent test: calculate GoF of the PC ν_μCC distributions after constraining the FC ν_μCC distributions. In this case, the common systematic uncertainties to the PC and FC channels are largely cancelled, and a
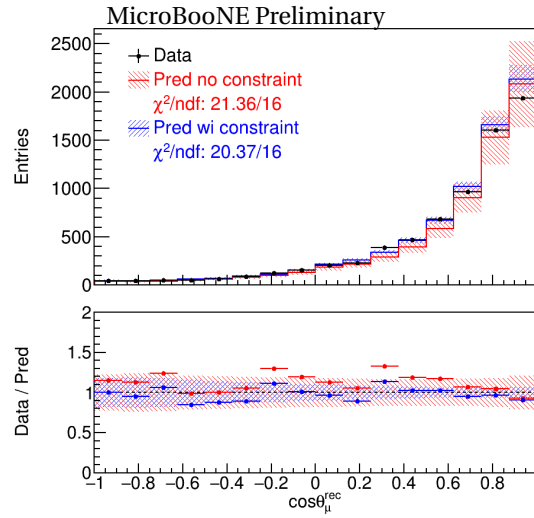
more stringent validation on the modeling of missing energy of PC events can be achieved.
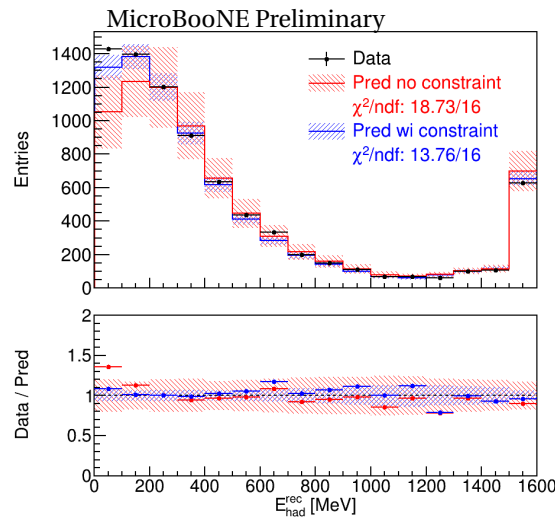
Figure 45 shows the comparison between data and prediction as a function of E_μ^{rec} for the PC events. After applying the constraints from the FC sample, the uncertainties of the prediction are significantly reduced. Nevertheless, the GoF values are still reasonable, indicating that the model describes the difference between FC and PC events very well. Figure 46 shows the comparison between data and prediction as a function of $\cos\theta_\mu^{rec}$ for the PC events. The GoF values (e.g. GoF = 20.4/16 with a p-value of 0.2) after applying constraints are still reasonable, indicating that the model describes the difference between FC and PC events well. We should note at the most forward muon angle, the prediction after constraints is enhanced, which slightly increase the difference between data and prediction. This change is the result of the fact that the data is higher than prediction in this bin for the FC events. Figure 47 shows the comparison between data and prediction as a function of E_{had}^{rec} for the PC events. The GoF values after applying constraints are still reasonable. In particular, we should note the prediction at the lowest bin of E_{had}^{rec} is enhanced after applying the constraints from the FC sample. This is expected since a similar behaviour is observed in the FC sample.

Figure 45: Comparison between data and prediction as a function of E_μ^{rec} for the partially contained events. The red (blue) lines and bands show the prediction without (with) the constraints from the fully contained event sample. The statistical, cross section, and flux uncertainties are included in the bands. The first 15 bins for 100 MeV per bin covers from 0.1 GeV to 1.6 GeV. The last bin is the overflow bin for events above 1.6 GeV.

Figure 46: Comparison between data and prediction as a function of reconstructed muon angle $\cos\theta_\mu^{rec}$ (relative to Z/beam). The red (blue) lines and bands show the prediction without (with) the constraints from the fully contained event sample. The statistical, cross section, and flux uncertainties are included in the bands. The 16 bins covers from -1 to 1.

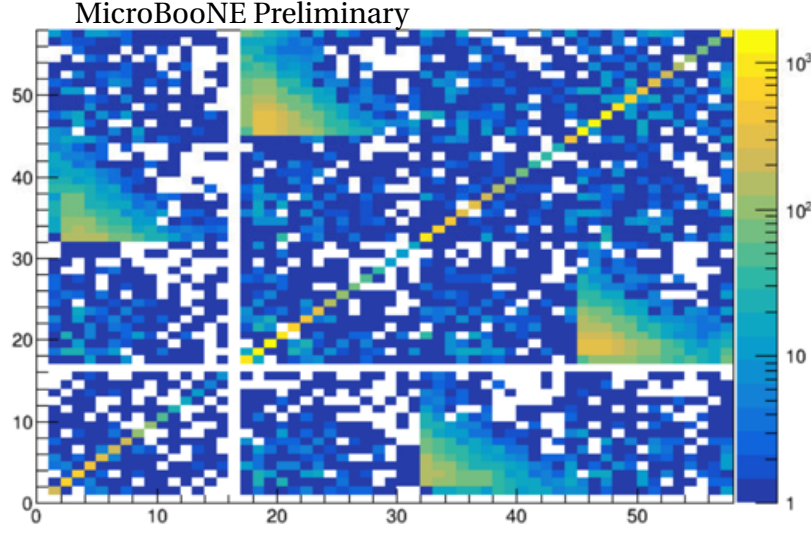**Figure 47:** Comparison between data and prediction as a function of the E_{had}^{rec}. The red (blue) lines and bands show the prediction without (with) the constraints from the fully contained event sample. The statistical, cross section, and flux uncertainties are included in the bands. The first 15 bins correspond to 0 GeV to 1.5 GeV. The last bin correspond to overflow bin above 1.5 GeV.

Figure 48: Comparison between data and prediction as a function of E_ν^{rec}. The red (blue) lines and bands show the prediction without (with) the constraints from the fully contained event sample. The statistical, cross section, and flux uncertainties are included in the bands. The first 25 bins with 100 MeV per bin correspond to the fully contained events from 0 GeV to 2.5 GeV. The 26th bin is the overflow bin corresponding to fully contained events above 2.5 GeV. The next 25 bins with 100 MeV per bin correspond to the partially contained events from 0 GeV to 2.5 GeV. The last bin is the overflow bin corresponding to the partially contained events above 2.5 GeV.

Finally, Fig. 48 shows the comparison between data and prediction as a function of E_ν^{rec} for the PC events. After applying the constraints from the FC sample, the uncertainties of the prediction are significantly reduced. Nevertheless, the GoF values are still reasonable, indicating that the model describes the difference between FC and PC events very well. With these results, we demonstrate that the model with its associated uncertainties can describe the difference between the PC and FC events (i.e. the missing energy that are outside the TPC active volume) well.
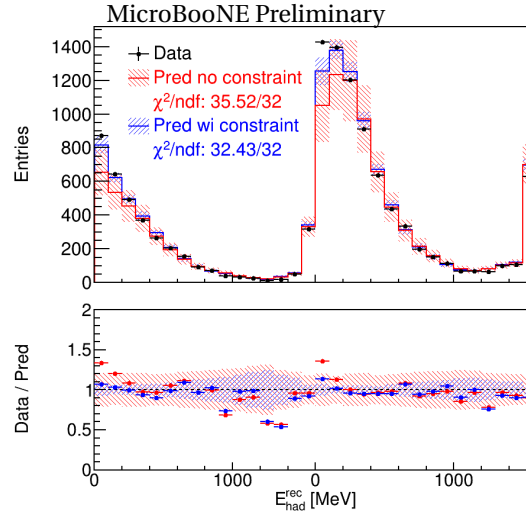
MicroBooNE Preliminary

Figure 49: Statistical covariance matrix constructed with the bootstrapping method [32]. Four blocks corresponding to i) FC ν_μCC E_μ distribution, ii) PC ν_μCC E_μ distribution, iii) FC ν_μCC E_{hadron} distribution, and iv) PC ν_μCC E_{had} distribution are shown. 5000 universes are used. There is no correlation between the FC and PC channels. For the same FC (PC) channel, there is a clear correlation between the E_μ and E_{had} distributions.

Similar to the situation of PC events, the reconstructed energy of the hadronic system E_{had}^{rec} cannot be directly mapped to the energy transfer to the Argon system, since some of the energy going into the neutron and low-energy gamma might be missing. In this case, the map of the E_{had}^{rec} to the energy transfer would rely on the overall model, particularly the cross section model. To validate the modeling of the these missing energies of the neutrons and low-energy gammas, a similar strategy using the conditional covariance matrix formalism is used. We examine the E_{had}^{rec} distribution after constraining the muon kinematics. In particular, we consider two one-dimensional muon kinematics: E_μ^{rec} and θ_μ^{rec}. If there is a new mechanism changing the behaviour of the missing energy in the hadronic system beyond the current model, a constraint in the muon kinematics (or distribution) will not change the data/MC difference in the distribution on E_{had}^{rec}, and the GoF will become much worse. For this examination, we use the bootstrapping method to estimate the correlated statistical uncertainties since the E_{had}^{rec} and $E_\mu^{rec}/\theta_\mu^{rec}$ distributions are from the same set of events. Figure 49 shows an example of statistical covariance matrix constructed with the bootstrapping method.
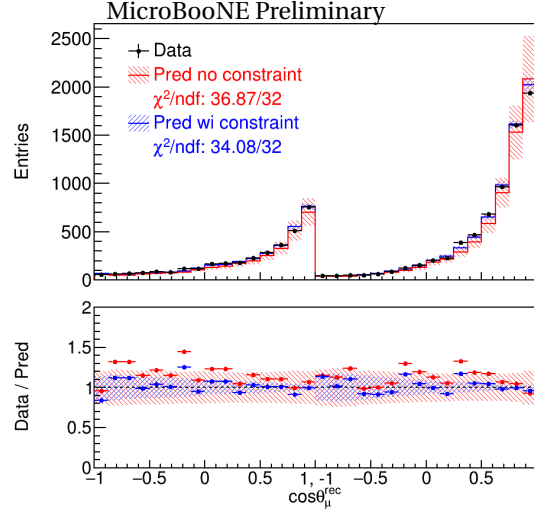
Figure 50 shows the comparison between data and prediction as a function of E_{had}^{rec} for both FC and PC events. After applying the constraints from the E_μ^{rec} distribution, the uncertainties of the prediction are significantly reduced. Nevertheless, the GoF values improve,

indicating that the model describes the relation between E_{had}^{rec} and E_{μ}^{rec} very well. In particular, we note the prediction at the lowest bin of E_{had}^{rec} is enhanced after applying the constraints from the E_{μ}^{rec} distribution. In another word, the differences between data and prediction in the E_{had}^{rec} distributions are significantly reduced, once the differences between data and prediction in the E_{μ}^{rec} distributions are eliminated within the allowed range of the model predictions.
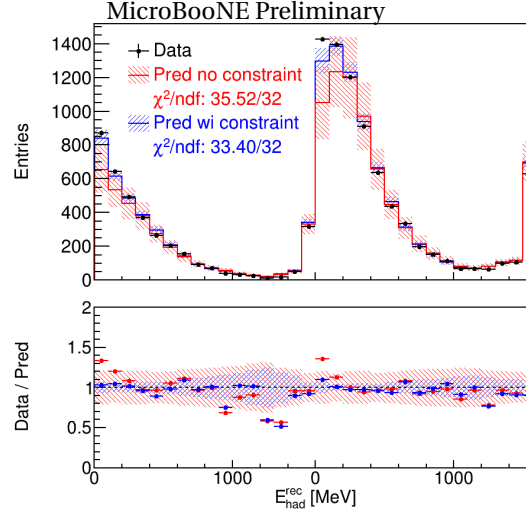

Figure 50: Comparison between data and prediction as a function of E_{had}^{rec}. The red (blue) lines and bands show the prediction without (with) the constraints from the distributions as a function of E_{μ}^{rec}. The statistical, cross section, and flux uncertainties are included in the bands. The first 15 bins with 100 MeV per bin correspond to the fully contained events from 0 GeV to 1.5 GeV. The 16th bin is the overflow bin corresponding to fully contained events above 1.5 GeV. The next 15 bins with 100 MeV per bin correspond to the partially contained events from 0 GeV to 1.5 GeV. The last bin is the overflow bin corresponding to the partially contained events above 1.5 GeV.

To further examine the E_{had}^{rec} distributions, we apply the constraints from the distributions of reconstructed muon angle. First, Fig. 51 shows the comparison between data and prediction as a function of $\cos\theta_{\mu}^{rec}$ for both FC and PC events. After applying the constraints from the E_{μ}^{rec} distribution, the uncertainties of the prediction are significantly reduced. Nevertheless, the GoF values (e.g. GoF = 34.1/32 with a p-value of 0.37) improve indicating that the model describes the relation between θ_{μ}^{rec} and E_{μ}^{rec} very well. The difference between data and predictions at the most forward angle ($\cos\theta_{\mu}^{rec} \sim 1$) is significantly reduced after applying the constraints from the E_{μ}^{rec} distribution. In another word, the differences between data and prediction in the $\cos\theta_{\mu}^{rec}$ distributions are significantly reduced, once the difference between data and prediction in the E_{μ}^{rec} distributions are eliminated within the allowed range of the model predictions.

Figure 51: Comparison between data and prediction as a function of $\cos\theta_\mu^{rec}$ (relative to Z/beam). The red (blue) lines and bands show the prediction without (with) the constraints from the reconstructed muon energy E_μ^{rec}. The statistical, cross section, and flux uncertainties are included in the bands. The first 16 bins correspond to the fully contained events covering from -1 to 1. The next 16 bins correspond to the partially contained events covering from -1 to 1.
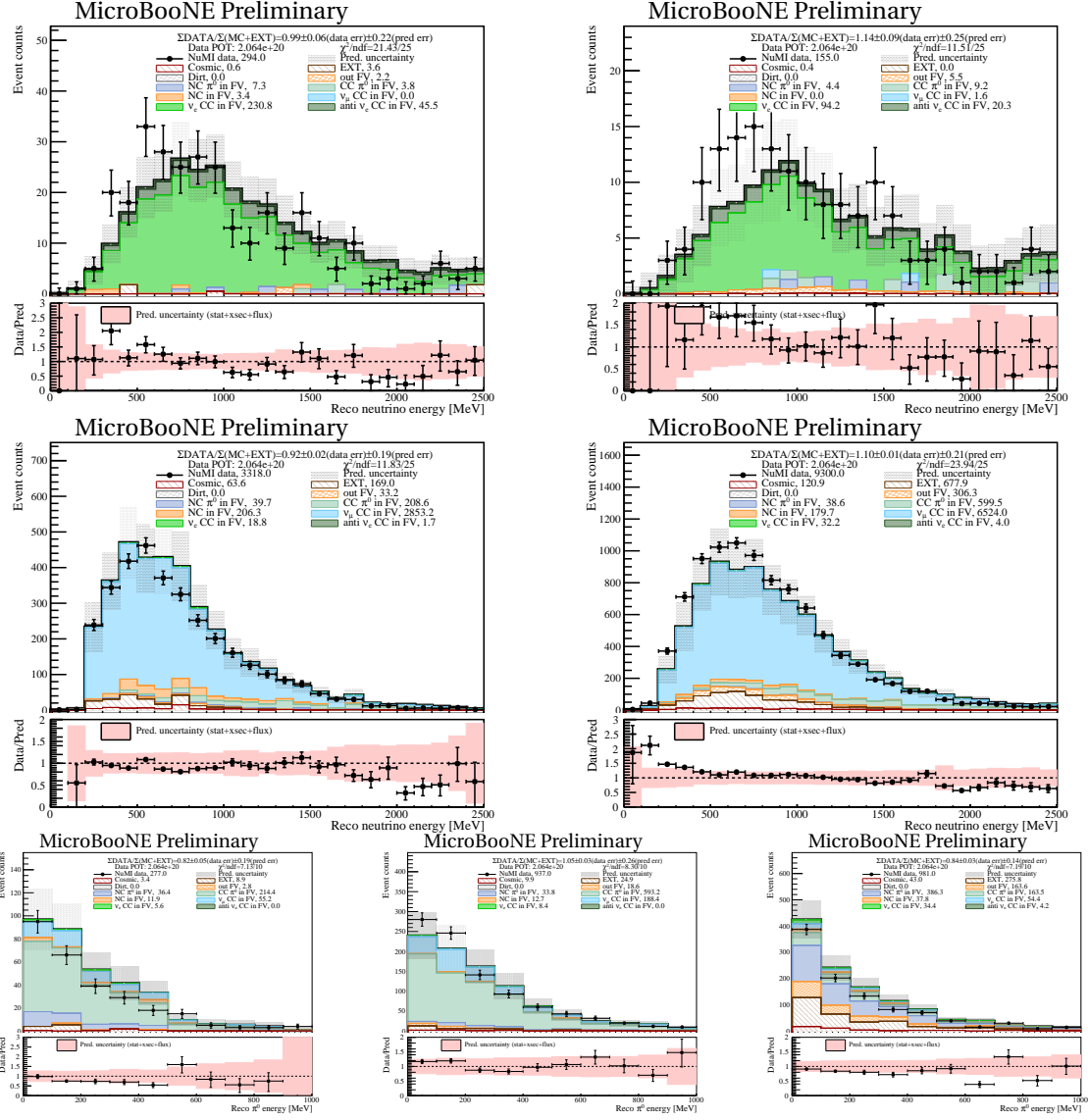
Next, we add the constraints from the distributions of reconstructed muon angle. Figure 52 shows the comparison between data and prediction as a function of E_{had}^{rec} for both FC and PC events. After applying the constraints from the E_μ^{rec} and $\cos\theta_\mu^{rec}$ distributions, the uncertainties of the prediction are significantly reduced. Nevertheless, the GoF values improve indicating that the model describes the relation between E_{had}^{rec} and the muon kinematics very well. In particular, we note the prediction at the lowest bin of E_{had}^{rec} is enhanced after applying the constraints from the E_μ^{rec} distribution. Compared to Fig. 50, the differences between data and prediction in the lowest bin of E_{had}^{rec} distributions are further reduced with the addition of constraints from reconstructed muon angle.

Figure 52: Comparison between data and prediction as a function of E_{had}^{rec}. The red (blue) lines and bands show the prediction without (with) the constraints from the reconstructed muon energy E_μ^{rec} and angle $\cos\theta_\mu^{rec}$. The statistical, cross section, and flux uncertainties are included in the bands. The first 15 bins with 100 MeV per bin correspond to the fully contained events from 0 GeV to 1.5 GeV. The 16th bin is the overflow bin corresponding to fully contained events above 1.5 GeV. The next 15 bins with 100 MeV per bin correspond to the partially contained events from 0 GeV to 1.5 GeV. The last bin is the overflow bin corresponding to the partially contained events above 1.5 GeV.

With these results, we demonstrate that the model with its associated uncertainties can describe the difference between the E_{had}^{rec} and the energy transfer to the argon nuclei $\nu = E_\nu - E_\mu$ (i.e. the missing energy associated with neutrons and low-energy gamma) well. We further elaborate on this point below. At the fixed true neutrino energy, the energy transfer to the Argon nuclei is associated with the muon kinematics. The difference between the energy transfer and the energy of the hadronic system is the missing energy. If the modeling of the missing energy with its uncertainties is incorrect, one would expect to see differences between data and predictions on the E_{had}^{rec} distributions after applying the constraints on the muon kinematics. Since we did not see such discrepancies in the E_{had}^{rec} distributions after applying constraints on the muon kinematics, we conclude that the current modeling of the missing energy because of neutrons and low-energy gammas is sufficient. These validations on the overall model provide a solid foundation in modeling the conversion from true neutrino energy to the reconstructed neutrino energy.
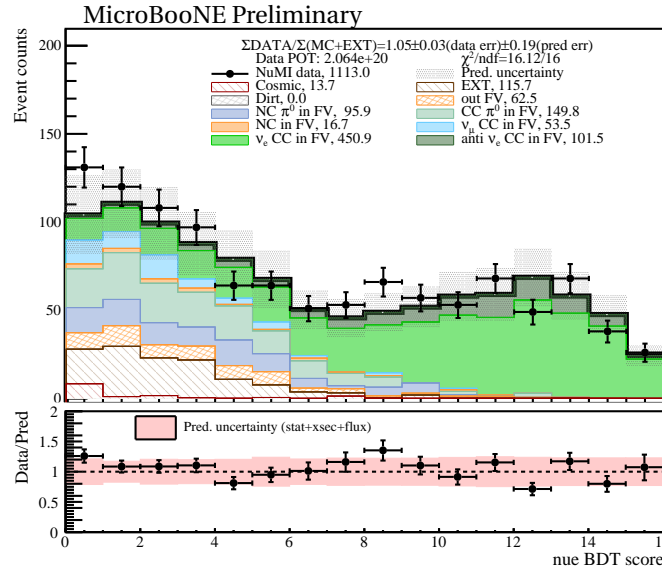
7 ANALYSIS OF NuMI DATA AT 2.06E20 POT

Figure 53: Distribution of 7-channel selection results from NuMI run1 data: (from left to right, top to bottom) fully contained ν_e CC, partially contained ν_e CC, fully contained ν_μ CC, partially contained ν_μ CC, fully contained CC π^0, partially contained CC π^0, and NC π^0. MC statistics, flux & cross-section uncertainty is included in the final uncertainty, shown in the red band in the panels below.

The current open data of the BNB data stream (~5.3e+19 POT) is limited by statistics, especially for FC ν_eCC channel at low-energy region. Such situation is not expected to change before the planned data unblinding at 6.95e+20 POT. Therefore,we are working on the data processing of the off-axis NuMI neutrino data stream, which is allowed for full access. At the same POT, the NuMI data stream has about three times more ν_eCC events than that of BNB
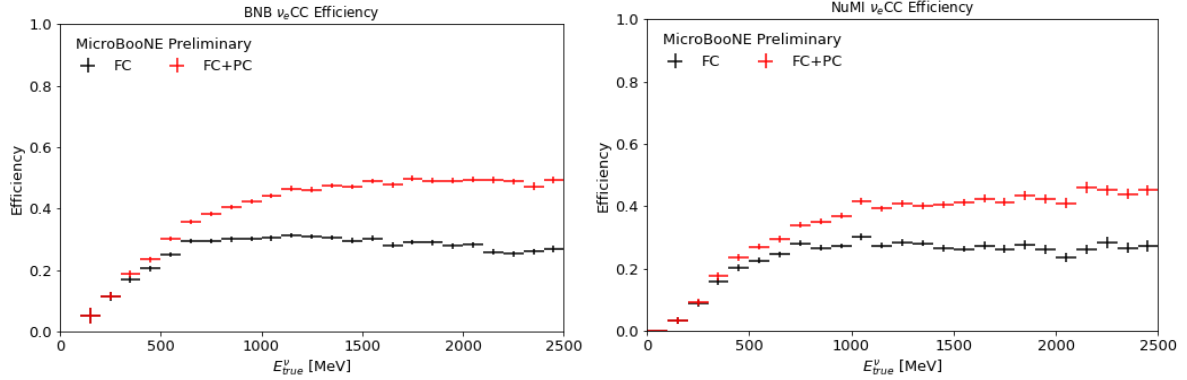
data stream in the low-energy region. The analysis of this channel is thus expected to provide useful information regarding the ν_eCC event selection. Figure 53 shows the result from the selections, for all the 7 channels. No changes were made on the event reconstruction, nor the event selection cuts (e.g. BDTs as in BNB ν_μCC and ν_eCC event selections). The only change is the coincidence window between the PMT flash with the trigger time (9 μs instead of 1.6 μs of BNB). The data/MC are consistent within systematic uncertainties. The distribution of nue BDT scores of NuMI events is presented in Fig. 54. It also shows a good agreement between data and Monte-Carlo, indicating the validity of the BNB ν_eCC BDT selection. Currently, the "Dirt" sample is not yet included, but given the purity of the selection on available Monte-Carlo samples, we expect its impact to be minimal. Nevertheless, future iterations of the analysis will include the study of this sample.
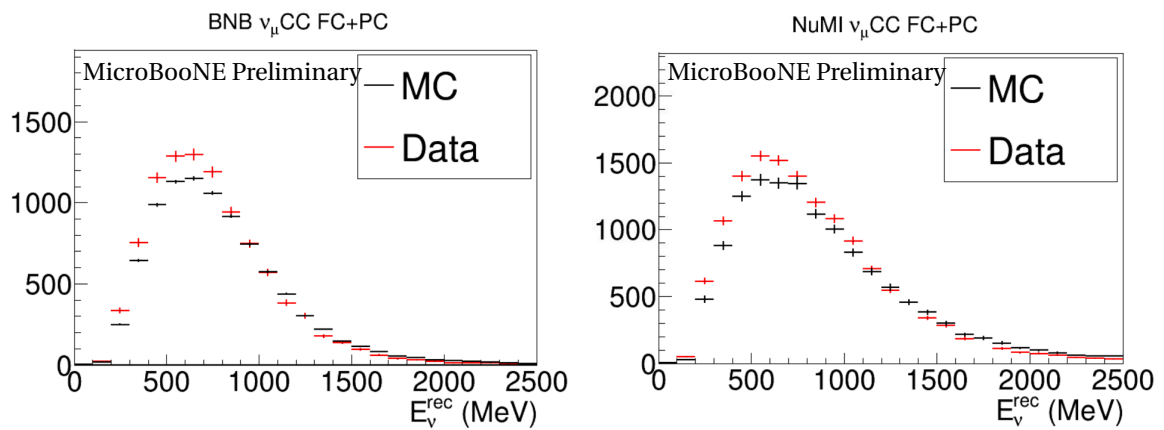

Figure 54: ν_e BDT score (greater than 0) distribution for both fully contained and partially contained event candidates. The NuMI data result is overlaid and the bottom panel presents the systematic uncertainty of the prediction, including MC statistic, cross section and flux uncertainties.

To demonstrate the similarity in the ν_eCC event selection, Fig. 55 shows ν_e selection efficiency comparison between BNB and NuMI data stream, as a function of true neutrino energy. The efficiency is comparable between two data streams, both in fully contained and combined samples, but slightly lower with NuMI FC sample compared to that of BNB. The data/MC consistency in the ν_eCC event selection from NuMI data validates the ν_eCC event selection strategy, and removes the potential concern that data/MC may have discrepancies in modeling ν_eCC events.
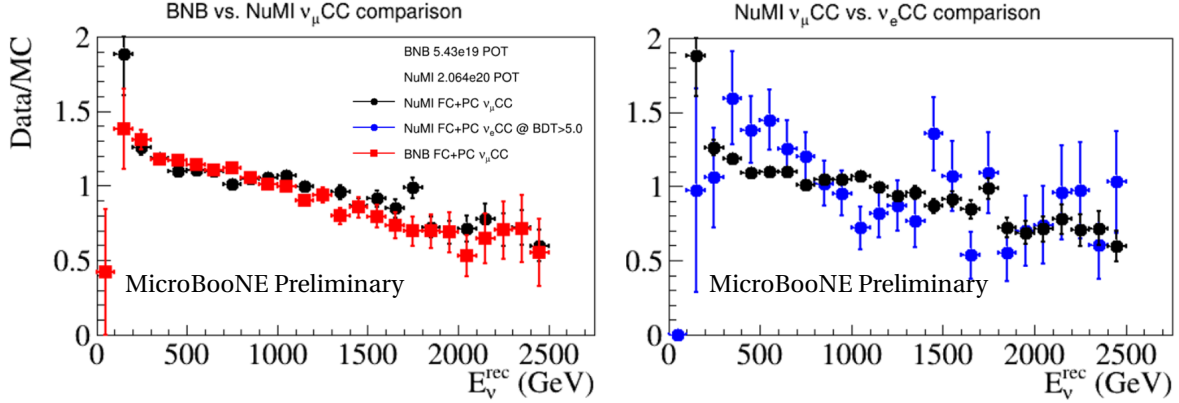
Figure 55: Selection efficiency of ν_eCC between BNB and NuMI data stream, as a function of true neutrino energy. The efficiency of NuMI data stream is slightly lower because the BDT was trained by BNB samples and directly applied on NuMI data.

Despite the success, there are two points worth commenting based on the observations in Fig. 53. The first point is that different behaviours between data and nominal Monte Carlo prediction are observed in FC ν_μCC sample from that of PC ν_μCC sample. This observation is different from that from the BNB data stream (see Fig. 33). The difference between the FC and PC channels in the NuMI data stream is because NuMI neutrino beam is no longer along the long-axis of the active TPC volume. With the different incident neutrino beam direction, the difference between data and nominal GENIE prediction (central value Monte Carlo) in terms of the primary muon kinematics (momentum and the polar angle) lead to the different behaviours between FC and PC samples. Once the FC and PC samples are combined, the data/MC comparison is similar between BNB and NuMI data stream (see Fig. 56).
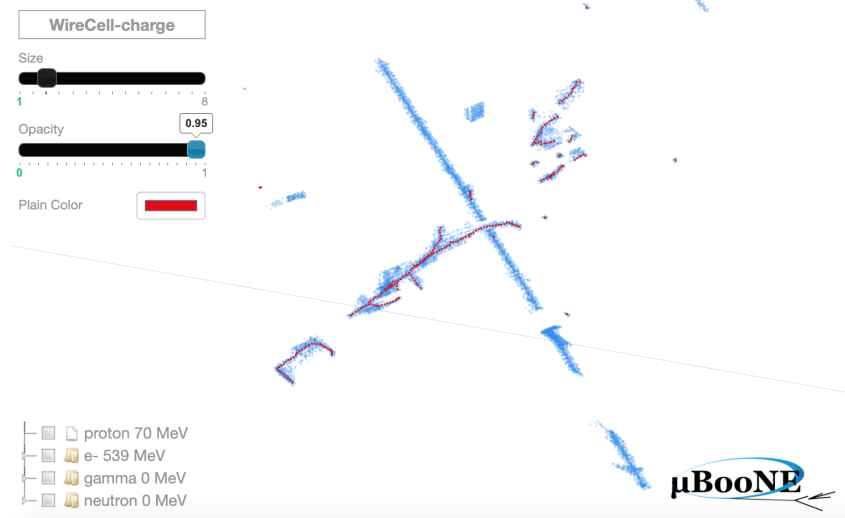

Figure 56: Comparison between data and MC with respect to the reconstructed neutrino energy after combining both FC and PC samples. (Left) BNB, (right) NuMI. Similar behaviours are observed.

Figure 57: Ratio of Data/MC as a function of reconstructed neutrino energy for different samples (ν_eCC and ν_μCC) from both BNB and NuMI data stream. To enhance the statistics of ν_eCC, we combined FC and PC samples as well as reducing the NuMI ν_eCC BDT cut value. See text for more discussions.

The second issue is regarding the difference between data and central value (or nominal) Monte Carlo prediction in the ν_eCC sample (See Fig. 53). Some excess (deficit) in data can be seen at low (high) energy region. To understand this point further, we plot the data/MC ratio as a function of the reconstructed neutrino energy for different samples (ν_eCC and ν_μCC) from both BNB and NuMI data stream in Fig. 57. There are some striking observations. The data/MC ratios for ν_μCC are consistent between the BNB and NuMI data stream. Second, within the limited statistics, the trend of NuMI ν_eCC is similar to that of the NuMI ν_μCC. This suggests that there is a common origin for this trend in data/MC ratio, which likely comes from the modelling of the neutrino-Argon interaction cross section, given the difference between the BNB and NuMI beam neutrino flavor content and kinematics distribution but the similarity observed in the data. To complete the analysis validation, we seek to understand the features of the NuMI nue spectrum with further exploration of the NuMI data and simulation. The overall conclusion we achieved in the NuMI analysis is consistent with that in Sec. 6.1.

In the end, to shed light on the slight excess of ν_eCC candidates around 600 MeV region, we hand scan the 400 - 800 MeV data events from the ν_eCC FC channel and ν_eCC PC channel in BEE display with a sub-sample, which corresponds to 1.874e20 POT NuMI data. None of the selected events show unexpected features. The links to the FC and PC channels are `https://www.phy.bnl.gov/twister/bee/set/uboone/reco/2021-01/numi-nue-fc-400-800-mev/event/list/` and `https://www.phy.bnl.gov/twister/bee/set/uboone/reco/2021-01/numi-nue-pc-400-800-mev/event/list/` respectively. An example ν_eCC candidate is shown below.

Figure 58: 1e1p FC ν_eCC. The blue space points are reconstructed clusters, and the red space points are fitted trajectory of the selected neutrino cluster. (`https://www.phy.bnl.gov/twister/bee/set/uboone/reco/2021-01/numi-nue-fc-400-800-mev/event/0/`)

8 SUMMARY

This technote summarizes the the current status of Wire-Cell eLEE analysis effort in MicroBooNE. With the BNB open data at 5.3e19 POT and NuMI data at 2.06e20 POT, a good data/MC consistency has been demonstrated for both ν_μCC and ν_eCC events on various variables. The reconstruction of neutrino energy and the overall model including all systematic uncertainties are validated for the upcoming eLEE search and cross section extraction. The robustness and the validity of the MicroBooNE Wire-Cell eLEE analysis strategy and method are demonstrated.

REFERENCES

[1] R. Acciarri et al. Design and Construction of the MicroBooNE Detector. *JINST*, 12(02):P02017, 2017.

[2] P. Abratenko et al. High-performance Generic Neutrino Detection in a LArTPC near the Earth's Surface with the MicroBooNE Detector. 12 2020.

[3] P. Abratenko et al. Cosmic Ray Background Rejection with Wire-Cell LArTPC Event Reconstruction in the MicroBooNE Detector. 1 2021.

[4] P. Abratenko et al. Neutrino Event Selection in the MicroBooNE Liquid Argon Time Projection Chamber using Wire-Cell 3-D Imaging, Clustering, and Charge-Light Matching. 11 2020.

[5] "Booster Neutrino Flux Prediction at MicroBooNE", MicroBooNE public-note 1031, `http://microboone.fnal.gov/wp-content/uploads/MICROBOONE-NOTE-1031-PUB.pdf`.

[6] "Supporting note: Cross-section model and uncertainties", `https://microboone-docdb.fnal.gov/cgi-bin/private/ShowDocument?docid=27018`.

[7] C. Adams et al. Ionization electron signal processing in single phase LArTPCs. Part I. Algorithm Description and quantitative evaluation with MicroBooNE simulation. *JINST*, 13(07):P07006, 2018.

[8] P. Abratenko et al. Measurement of space charge effects in the MicroBooNE LArTPC using cosmic muons. *JINST*, 15(12):P12037, 2020.

[9] C. Adams et al. Calibration of the charge and energy loss per unit length of the MicroBooNE liquid argon time projection chamber using muons and protons. *JINST*, 15(03):P03022, 2020.

[10] "Measurement of the Electronegative Contaminants and Drift Electron Lifetime in the MicroBooNE Experiment", MicroBooNE public note 1003, `http://microboone.fnal.gov/wp-content/uploads/MICROBOONE-NOTE-1003-PUB.pdf`.

[11] C. Adams et al. Ionization electron signal processing in single phase LArTPCs. Part II. Data/simulation comparison and performance in MicroBooNE. *JINST*, 13(07):P07007, 2018.

[12] R. Acciarri et al. Noise Characterization and Filtering in the MicroBooNE Liquid Argon TPC. *JINST*, 12(08):P08003, 2017.

[13] A. A. Aguilar-Arevalo et al. Significant Excess of ElectronLike Events in the MiniBooNE Short-Baseline Neutrino Experiment. *Phys. Rev. Lett.*, 121(22):221801, 2018.

[14] "MicroBooNE low-energy excess signal prediction from unfolding MiniBooNE Monte-Carlo and data", MicroBooNE public note 1043, `http://microboone.fnal.gov/wp-content/uploads/MICROBOONE-NOTE-1043-PUB.pdf`.

[15] Gary J. Feldman and Robert D. Cousins. A Unified approach to the classical statistical analysis of small signals. *Phys. Rev. D*, 57:3873–3889, 1998.

[16] P. Abratenko et al. Cosmic Ray Background Rejection with Wire-Cell LArTPC Event Reconstruction in the MicroBooNE Detector. 1 2021.

[17] PSTAR at NIST: `https://physics.nist.gov/PhysRefData/Star/Text/PSTAR.html`.

[18] P. Abratenko et al. Neutrino Event Selection in the MicroBooNE Liquid Argon Time Projection Chamber using Wire-Cell 3-D Imaging, Clustering, and Charge-Light Matching. 11 2020.

[19] Tianqi Chen and Carlos Guestrin. XGBoost: A Scalable Tree Boosting System. 3 2016.

[20] Monte Carlo Statistical Uncertainties, W. Gu et al., MicroBooNE doc-db 32714.

[21] MicroBooNE Flux Uncertainty Implementation, Z. Pavlovich and J. Zennamo, MicroBooNE doc-db 8622.

[22] Cross-section model and uncertainties, K. Duffy, S. Dytman, and S. Gardiner, MicroBooNE doc-db 27018.

[23] A.A. Aguilar-Arevalo et al. The Neutrino Flux prediction at MiniBooNE. *Phys. Rev. D*, 79:072002, 2009.

[24] Geant4 systematics: eventweight module validation, Kirsty Duffy, MicroBooNE doc-db 27561.

[25] Xiangpan Ji, Wenqiang Gu, Xin Qian, Hanyu Wei, and Chao Zhang. Combined Neyman–Pearson chi-square: An improved approximation to the Poisson-likelihood chi-square. *Nucl. Instrum. Meth. A*, 961:163677, 2020.

[26] T. Hauschild and M. Jentschel. Comparison of maximum likelihood estimation and chi-square statistics applied to counting experiments. *Nucl. Instrum. Meth.*, A457:384–401, 2001.

[27] Morris L Eaton. Multivariate statistics: a vector space approach. *John Wiley and Sons*, pages 116–117, 1983.

[28] New Method for Applying the ν_μ Constraint on the ν_e Cov-Matrix and Prediction, X. Qian, M. Toups, and M. Shaevitz, MicroBooNE doc-db 32672.

[29] P. Abratenko et al. First Measurement of Inclusive Muon Neutrino Charged Current Differential Cross Sections on Argon at E_ν ~0.8 GeV with the MicroBooNE Detector. *Phys. Rev. Lett.*, 123(13):131801, 2019.

[30] P. Abratenko et al. Measurement of Differential Cross Sections for ν_μ-Ar Charged-Current Interactions with Protons and no Pions in the Final State with the MicroBooNE Detector. *Phys. Rev. D*, 102(11):112013, 2020.

[31] P. Abratenko et al. First Measurement of Differential Charged Current Quasielastic-like ν_μ-Argon Scattering Cross Sections with the MicroBooNE Detector. *Phys. Rev. Lett.*, 125(20):201803, 2020.

[32] Bootstrapping (statistics). `https://en.wikipedia.org/wiki/Bootstrapping_ (statistics)`. Accessed: 2021-02-17.